UC Merced
UC Merced Electronic Theses and Dissertations

Title
Architected Conducting Polymers

Permalink
https://escholarship.org/uc/item/3zt913sj

Author
Frye, Jacob

Publication Date
2020

Peer reviewed|Thesis/dissertation

UNIVERSITY OF CALIFORNIA MERCED

Architected Conducting Polymers

A Thesis submitted in partial satisfaction of the requirements
for the degree of Master of Science

in

Materials and Biomaterials Science and Engineering

by

Jacob Frye

Committee in charge:

Professor Sarah Kurtz, Chair

Professor Ashlie Martini

Professor Christopher Viney

Professor Yue (Jessica) Wang, Advisor

The Thesis of Jacob Frye is approved, and it is accepted
in quality and form for publication on microfilm and electronically:

_____

Professor Sarah Kurtz, Chair

_____

Professor Ashlie Martini

_____

Professor Christopher Viney

_____

Professor Yue (Jessica) Wang, Advisor

University of California, Merced

2020

Contents

Abstract

Conducting polymers offer the ability to create electronic devices that are lightweight with relatively simple processing compared to their inorganic counterparts. They have recently gained attention in the wearable electronics field due their ability to exhibit flexibility and low stiffness while conducting electricity. However, conducting polymers are not intrinsically flexible and must be modified, usually at the expense of electrical performance, or through the use of expensive and toxic additives. Here, we explore the use of architected materials to tune a conductive polymer's mechanical properties without chemical modification. To do so, a reliable and high-throughput 3D printing system for a conducting polymer-based hydrogel was established. The system utilizes a stereolithography apparatus (SLA) to 3D print a hydrogel of almost any 3D shape. The hydrogel acts as a dopant and structural component for a subsequently grown conducting polymer. This means a conducting polymer, which is usually limited to being a thin film or a stochastic foam, can be made into specific and complex geometries, enabling the tailoring of its mechanical properties through architecture, without compositing or chemical modification. When architected into a lattice, the conducting polymers can withstand compressive strain up to 80% without failure, whereas their bulk counterpart reaches just 25% strain before undergoing brittle fracture. The architected conducting polymers also exhibit a strain rate invariant stress-strain curve, suggesting that a potential strain rate invariant electrical resistance behavior may exist, but further investigation is required.

I. Introduction

Since their initial discovery in the 1970s, conducting polymers, often considered "plastics that conduct electricity," have attracted a great deal of interest from all disciplines of science and engineering due to their low density compared to metals, synthetic nature that eliminates mining, and chemically tunable physical properties. Throughout the past several decades, their electrical, mechanical and optical properties have been thoroughly investigated, often in relation to chemical modification of polymer backbones, and to processing methods. This arsenal of fundamental knowledge has transformed these organic conductors from a scientific curiosity to materials enabling transformative new technologies in electronics such as organic light emitting diode (OLED) displays, lightweight and flexible organic solar cells (OPV). [1,2]

In recent years, new electronic technologies such as devices that can be woven into clothes, directly attached to our skin, incorporated with soft robotics as functional prosthetics, or even implanted in our bodies, has brought a new wave of excitement to this rapidly evolving field. In addition to convenience, these electronics blur the line between human and machine, and offer unprecedented opportunities for health monitoring due to their possible use in intimate contact with the human body. However, with new opportunities, there come new challenges.

The human body constantly undergoes a large variety of mechanical motion, including bending, stretching, compression, twisting, over a large range of speeds. Direct interfacing of electronics with such an entity entails that the electronics need to be able to deform and recover under the same type of motion and rate while maintaining stable performance. Furthermore, these devices need to be soft like skin or tissue, which are not characteristic properties of current electronic materials. The emerging field of "stretchable electronics" or "deformable electronics" aims to make such technological breakthroughs.

A variety of approaches have been taken to make stretchable/deformable electronics such as island-interconnects, where small islands of rigid electronics are connected with compliant, conductive materials, like low temperature liquid metals, soft polymers, or even rigid metals (**Figure 1.1**). [3,4,5] The rigid metals in this case achieve compliance through out-of-plane buckling, which is a result of their geometry. Other approaches, such as kirigami and origami, utilize sheets with designed buckling regions that allow the material to alternate between bistable states (**Figure 1.2**).[6] Some approaches solely use conducting polymers. However, conducting polymers are intrinsically brittle as a result of their rigid backbones, and need to be modified to exhibit reversibly deformable properties. [7]
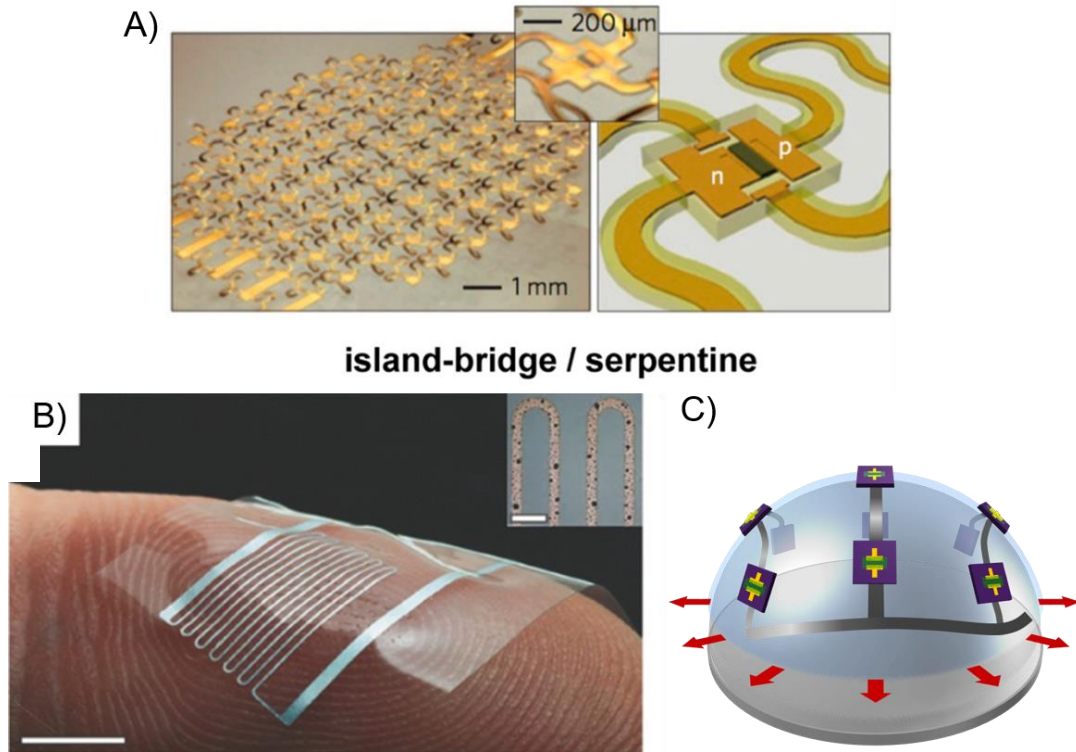
Figure 1.1. Island-interconnects made with A) solid metal, B) liquid metal, and C) a conducting polymer. (Adapted from ref. 3, 4 and 5, respectively.)

Figure 1.2. Origami-inspired wearable electronics. (Adapted from ref. 6.)

Like other polymers, conducting polymers can be tailored to be stretchable via chemical modification. Special care must be taken to preserve the molecular structure that enables conduction, often requiring complex processes and expensive additives.[5] Another method to increase the stretchability or deformability of conducting polymers is

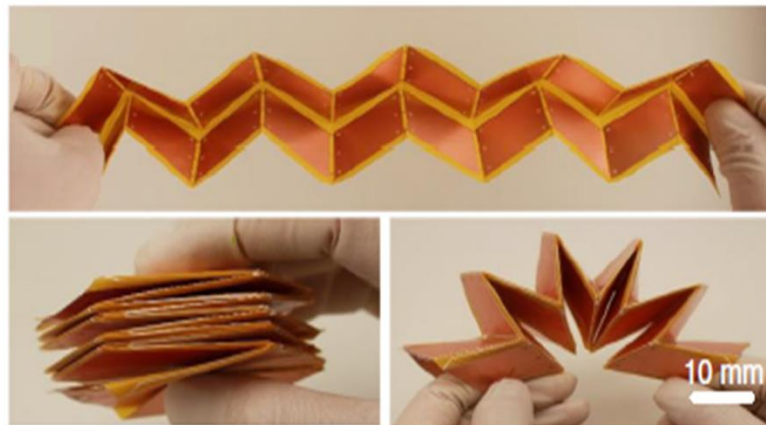depositing them as a thin film onto an elastic substrate with much higher thickness, where the stresses that arise when the material is under strain are mostly placed on the substrate than on the conducting polymer thin film.[8] However, special consideration must be taken for the implementation of the thin film – substrate system, as it is only beneficial with certain types of loading, and can otherwise lead to out-of-plane deformation.[9] Bao et al. created a stochastic foam made from a conducting polymer, where the 3D microporous network afforded a compliant structure.[9] Conducting polymer foams have the advantage of being very light weight and being able to maintain a constant electrical resistance under compressive and tensile loads. However, the mechanical properties are the average properties of the foam. With large variation in pore sizes and cell wall thicknesses, fine tuning the mechanical properties can be difficult. The work in this thesis explores well-defined lattice structures as a new method of tailoring the mechanical properties of a conducting polymer, without any chemical modification or additives.

Recent advances in 3D printing technology have enabled the creation of materials of complex geometries at ultra-fine scales at relatively low cost. This has helped expand the study of the decades-old idea of materials with non-intrinsic behaviors as a direct result of their geometry (metamaterials): brittle and stiff materials enduring and recovering from compression of up to 35-percent strain, negative Poisson's ratio, and compliant mechanisms for motion and mechanical logic (**Figure 1.3**).[10,11,12] In addition to the uniquely behaving materials, lattice materials have demonstrated the ability to achieve higher strength-to-weight performance over their full-density counterparts.[13] Lattice materials are a type of cellular material with a regular repeated unit cell, similar to crystal lattices. Unlike other cellular materials such as stochastic foams, lattice materials are composed of well-defined beam elements in specific arrangements (**Figure 1.4**). Their mechanical properties are a result of the geometries and connectivity of the beam elements. The prominent impact that lattice materials have had is their expansion of property space; filling in gaps and pushing the boundaries of performance into the upper vacant region of strength vs. density Ashby plots (**Figure1.5)**.[13]

This new knowledge of the architecture-property relationships opens exciting avenues towards creating new properties from old materials purely through structural design, and poses as an appealing approach to transform the brittle conducting polymers into stretchable, compressible, or even elastic materials for next-generation electronics applications. Being able to tune a material's mechanical properties by simply controlling its spatial distribution is attractive because it extends the range of properties that existing well-studied materials can obtain, without the complexities of compositing or chemical modification. It also opens up the possibility for conducting polymers to forgo any additives that can be expensive and toxic. The challenge, however, lies in the development of a system that can create the complex geometries (e.g. structure in **Figure 1.4B**) that provide the enhancement of mechanical properties.
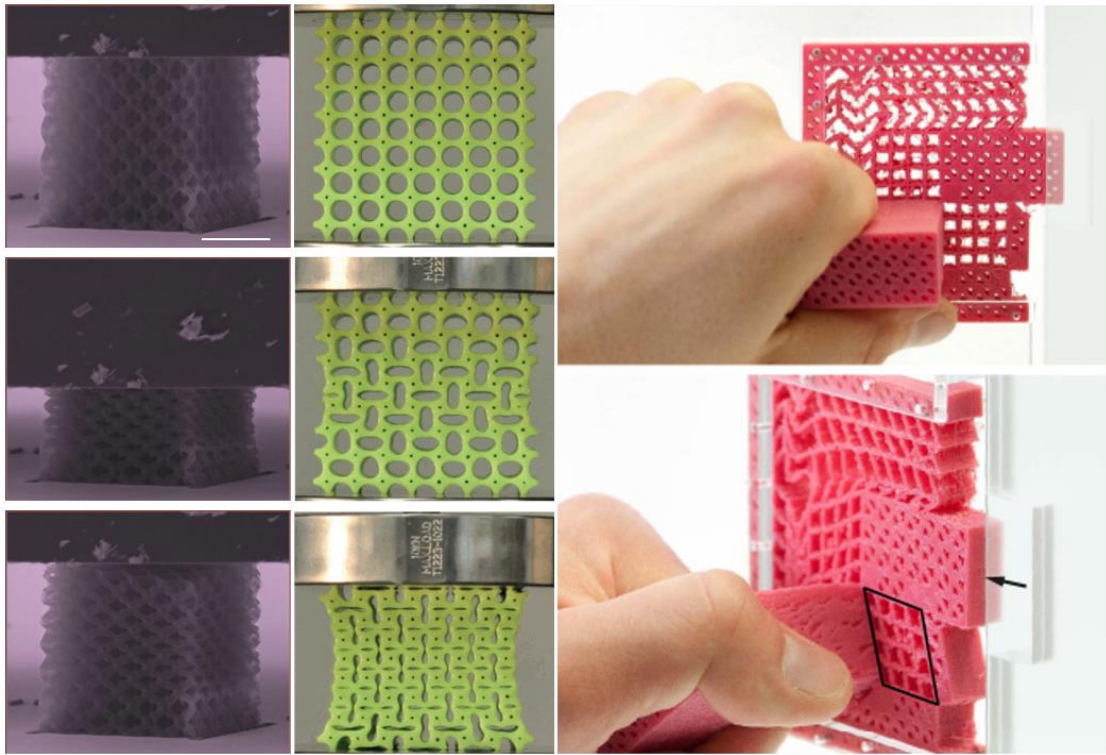
Figure 1.3. A) An alumina nanolattice being compressed to 35% strain, and its subsequent recovering (scale bar = 10 μm). B) An elastomeric 2D lattice exhibiting a negative Poisson's ratio during compression. C) A 3D printed door handle and latch with selective regions of compliance and stiffness to enable it to operate while being made of a single piece of material. (Adapted from ref. 10, 11 and 12, respectively.)

Figure 1.4. A) stochastic (or random) foam. B) A truncated octahedron lattice. (1.4A adapted from ref. 9)

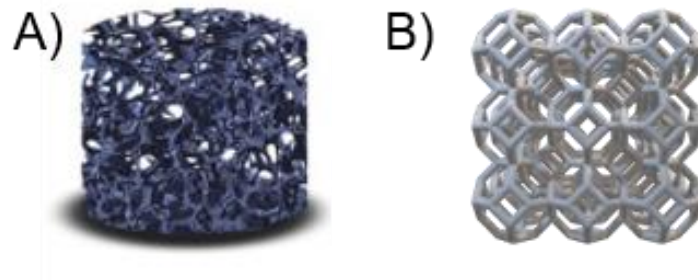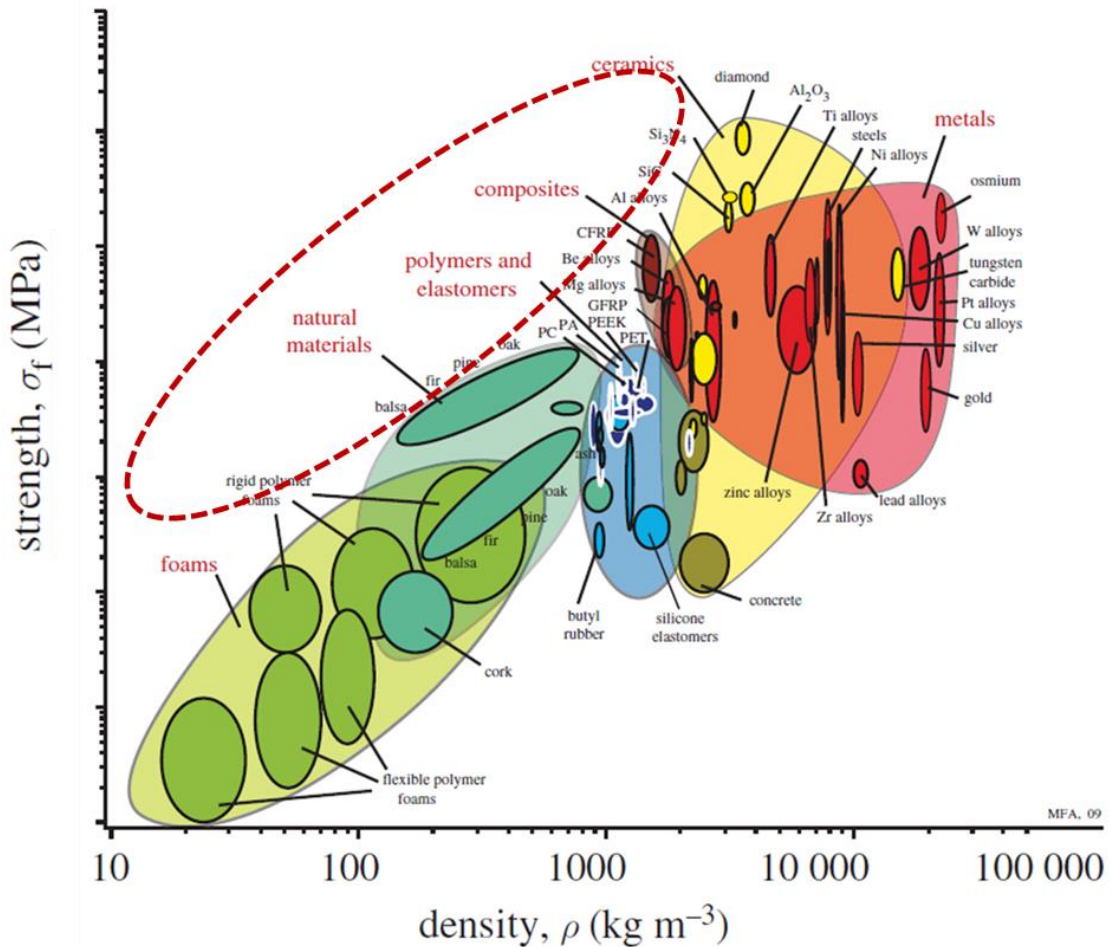**Figure 1.5**. The upper vacant regions of a strength vs. density Ashby plot, encircled by a red dashed line. The vacant region represents highly desirable materials with high strength-to-density ratios. (Adapted from ref. 13.)

I.1. 3D Printing Methods

The three most common 3D printing methods are fused deposition modeling (FDM), photopolymerization (stereolithography and digital light projection), and selective laser sintering (SLS) (**Figure 1.6**). FDM involves the extrusion of a thermoplastic filament, heated beyond its melting temperature, to build 3D objects layer by layer. While FDM is the most commonly available 3D printing system, it is difficult to implement for conducting polymers, as melt processing typically leads to oxidation and loss of conductive properties. In addition, with FDM it is difficult to print 3D lattice materials without support structures, and support structures are extremely difficult to remove from 3D lattice materials. SLS utilizes a laser to sinter, layer by layer, a powder bed of plastic

5

or metal. SLS has the advantage of a wider material variety, high resolution, and the ability to print without needing support structures. However, like with FDM, the mechanism for fusing material is not compatible with known conducting polymers, due to their thermal instabilities. The chemical instability of conducting polymers is one of the main reasons for the scarcity of 3D printing literature on these technologically important materials despite the rapid proliferation of the 3D printing field as a whole. However, light-based 3D printing methods such as SLA or DLP offer a hopeful glimpse into this possibility. SLA and DLP utilize a laser (commonly near-UV) to initiate photopolymerization via (but not limited to) a radical species within a resin of monomers, oligomers and photoinitiators. The laser is rastered in a 2D pattern, curing a thin layer of resin, and is repeated until a 3D object is formed. Photopolymerization is a viable method for making 3D printed conducting polymers, but the direct polymerization of a conducting polymer during printing is currently difficult to do, as conducting polymers can strongly absorb in the spectrum of the light source and scavenge radicals. Therefore, the conducting polymer is usually grown in a post print process.[14a]
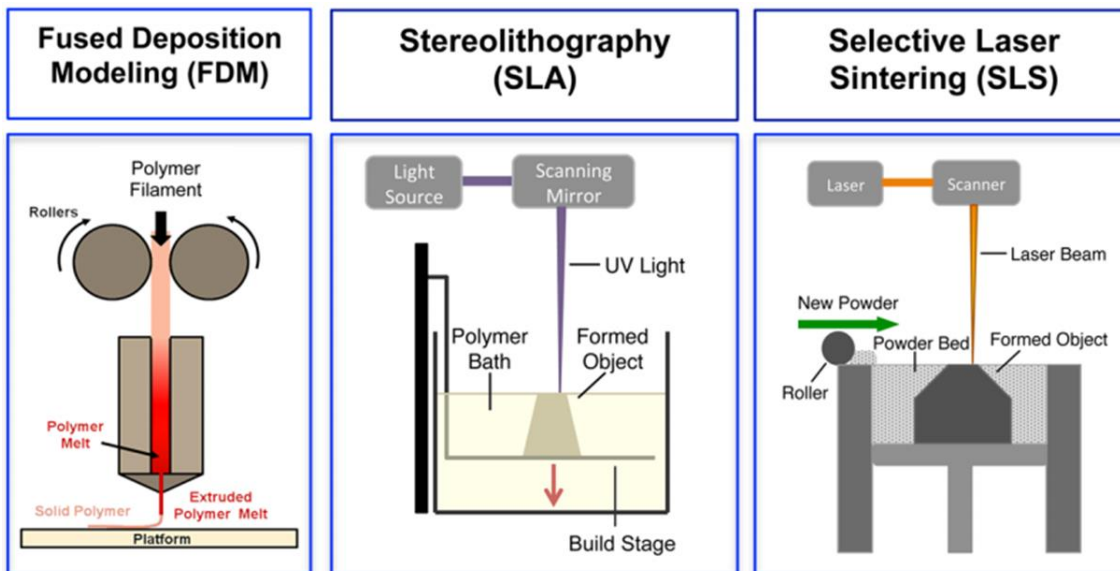

Figure 1.6. The three most common 3D printing methods. (Adapted from ref. 15.)

Among the sporadic publications on 3D printed conducting polymers, recent proof-of-concept work done by Fantino et al. demonstrates the feasibility to create complex 3D architected structures of this class of materials. They utilized a DLP system to 3D print a poly(ethylene glycol)diacrylate/polypyrrole (PEGDA/PPY) conducting hydrogel via a two-step process.[14b]
First, they used a DLP system to print complex 3D structures of PEGDA hydrogel, a commonly used insulating polymer in SLA/DLP printing, as a structural scaffold (**Figure 1.7**). The PEGDA hydrogel is subsequently swelled in an aqueous solution of $FeCl_3$, and then placed into a pyrrole in cyclohexane solution for oxidative polymerization. The

PEGDA hydrogel support structure acts as a medium to load the oxidant. The PPY monomers are dissolved into cyclohexane, which is immiscible with water in the hydrogel. This allows polymerization to occur entirely within the hydrogel when the PPY monomers diffuse into it. The result is a complex 3D structure made of a composite hydrogel containing both the insulating PEGDA and conductive PPY.

In comparison to Fantino's work, our work overlaps with the method of growing a conductive polymer within a 3D printed hydrogel to make it electrically conducting. While their approach is certainly interesting and clever, a dye was used as a dopant, which is separate from the hydrogel, and the PEGDA hydrogel acts only as a structure, decreasing the portion of material to participate in electrical conduction. Our work differentiates itself by the utilization of a novel resin to create a hydrogel that acts as a support structure *and* actively plays a role in electrical conduction. In addition, the complex 3D structures made in our work were used to investigate the efficacy of tailoring the mechanical properties of a conducting polymer with architecture.
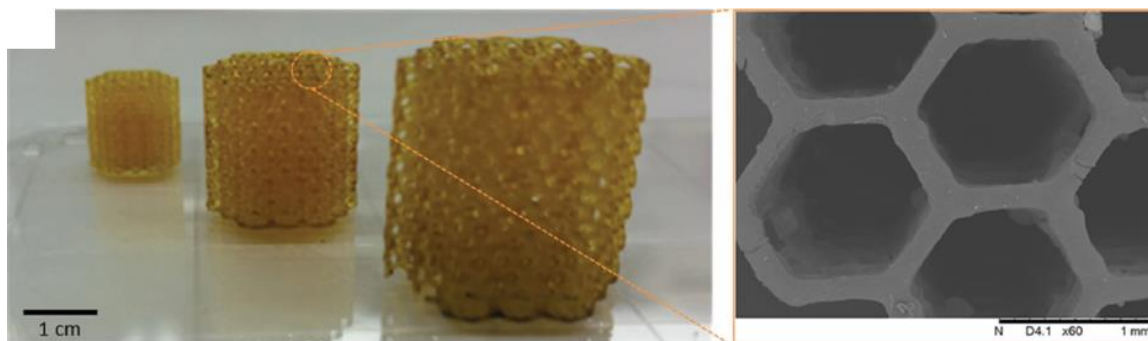

Figure1.7. A complex 3D honeycomb PEGDA hydrogel. (Adapted from ref. 14b.)

I.2. Goals

There were three main goals for the project. The first goal was to establish a reliable 3D-printing platform that can produce complex 3D architectures of conducting polymer hydrogels without an insulating polymer network purely for structural support. The second goal was to determine the viability of architected lattice materials' role in tailoring the mechanical properties of a conducting polymer. In addition, it was desired to characterize the effect with two well-known architectures to establish a property scaling function for fine-tuning the mechanical properties and behavior. The third goal was to establish a correlation between electrical and mechanical properties for each architecture. Furthermore, the hydrogels are a pathway to the ultimate goal of a solid-state conducting polymer whose mechanical properties are tailored with architecture, without the need of compositing or chemical modification.

I.3. Approach

Our approach described below is novel in two ways. First, the structural component that is 3D printed consists primarily of a polymer that serves as a dopant for the conductive polymer. This allows for most of the structure to play a role in conduction, eliminating the need to incorporate a structural polymer with no contribution to electrical properties. The second novelty is the tailoring of mechanical properties purely through architecture design, without the need for harsh and expensive chemical additives with unknown environmental effects or complex synthetic procedures for molecular modification. The implementation of lattice materials provides the ability to expand the property space of well-known materials/chemistries.

References

1. H. Sirringhaus, Adv. Mater. **2014**, 26, 1319.

2. J. Chen, Y. Cao, Acc. Chem. Res. **2009**, 42(11), 1709.

3. R. Kim, D. Kim, J. Xiao, B. H. Kim, S. Park, B. Panilaitis, R. Ghaffari, J. Yao, M. Li, Z. Liu, V. Malyarchuk, D. G. Kim, A. Le, R. G. Nuzzo, D. L. Kaplan, F. G. Omenetto, Y. Huang, Z. Kang, J. A. Rogers*, Nature Mater* **2010**, *9, 929-937.*

4. M. D. Dickey, *Adv. Mater.* **2017**, *29, 1606425.*

5. Y. Wang, C. Zhu, R. Pfattner, H. Yan, L. Jin, S. Chen, F. Molina-Lopez, F. Lissel, J. Liu, N. I. Rabiah, Z. Chen, J. Chung, C. Linder, M. F. Toney, B. Murmann, Z. Bao, *Sci. Adv.* **2017**;3: e1602076

6. K. Tao, H. Yi, Y. Yang, L. Tang, Z. Yang, J. Wu, H. Chang, and W. Yuan, *Microsystems & Nanoengineering* **2020**, *6, 56.*

7. S. E. Root, S. Savagatrup, A. D. Printz, D. Rodriquez, and D. J. Lipomi, *Chem. Rev.* **2017**, *117, 6467-6499.*

8. E. J. Sawyer, A. V. Zaretski, A. D. Printz, N. V. de los Santos, A. Bautista-Gutierrez, D. J. Lipomi, *Extreme Mechanics Letters*, **2016**, *8, 78-87.*

9. G. Chen, R. Rastak, Y.Wang, H. Yan, V. Feig, Y. Liu, Y. Jiang, S. Chen, F. Lian, F. Molina-Lopez, L. Jin, K. Cui, J. Chung, E. Pop, C. Linder, and Z. Bao, *Matter* **2019**, *1, 205-218.*

10. L. R. Meza, L. Das, and J.R. Greer*, Science* **2014**, *345, 6202.*

11. J. T. B. Overvelde, S. Shan, and K. Bertoldi, *Adv. Mater.* **2012**, *24, 2337-2342.*

12. A. Ion, J. Frohnhofen, L. Wall, R. Kovacs, M. Alistar, J. Lindsay, P. Lopes, H. Chen, and P. Baudisch, *Proceedings of UIST'16* **2016**, *16-19.*

13. N. A. Fleck, V. S. Deshpande, and M. F. Ashby*, Proc. R. Soc. A.* **2010**, *466, 2495-2516.*

14. R. Jordan, Y. Wang, *Journal of Polymer Science, Part B: Polymer Physics* 2019, 57, 1592–1605, 14a) Y. Wu, Y. X. Chen, J. Yan, S. Yang, P. Dong, P. Soman, *J. Mater. Chem. B* **2015**, *3, 5352.* 14b) E. Fantino, I. Roppolo, D. Zhang, J. Xiao, A.

Chiappone, M. Castellino, Q. Guo, C. F. Pirri, J. Yang, Macromol. Mater. Eng. 2018, 303, 1700356.

15. M. Guvendiren, J. Molde, R. M. D. Soares, J. Kohn, ACS Biomater. Sci. Eng. **2016**, 2, 1679.

II. 3D Printing System

Creating architected structures of conducting polymers via SLA printing requires the development and optimization of a multitude of components. The photopolymerization mechanism behind SLA requires the formulation of a resin that can turn monomers, oligomers and crosslinkers into a solid polymer within a fraction of a second and only along the laser rastering pathway (II.1). The 3D architecture needs to be designed and deconstructed into 2D slices by a couple of different software (II.2). Modification of the commercial SLA printer is essential for enabling the printing of our custom resin (II.3). Finally, the printing and post-processing processes need to be optimized (II.4).

II.1. Resin

The SLA resin is an aqueous solution of monomers, sodium 2-Acrylamido-2-methyl-1-propanesulfonic acid (Na-AMPSA) and acrylamide; a crosslinker, *N,N'*-Methylenebis(acrylamide) (MBAA); a photoinitiator, sodium phenyl(2,4,6-trimethylbenzoyl)phosphinate (Na-TPO); and a dye, quinoline yellow (**Figure 2.1**). The anionic AMPSA plays a dual role of forming a structural component and a doping polymer to the cationic polyaniline. The function of the acrylamide is to reduce the swelling of AMPSA when hydrated, while providing additional toughness. Without the acrylamide, the purely AMPSA hydrogels are brittle as a result of their large degree of swelling, making them difficult to handle, and limiting their practicality. Na-TPO is a water-soluble photoinitiator that absorbs in the spectrum of the most commonly used light source of light-based 3D printers (405 nm). Quinoline yellow is a common food dye that strongly absorbs 405 nm light and serves to limit laser penetration, which reduces over-crosslinking and line width spreading. **Figure 2.1** provides an illustration of the hydrogel network and its constituents.
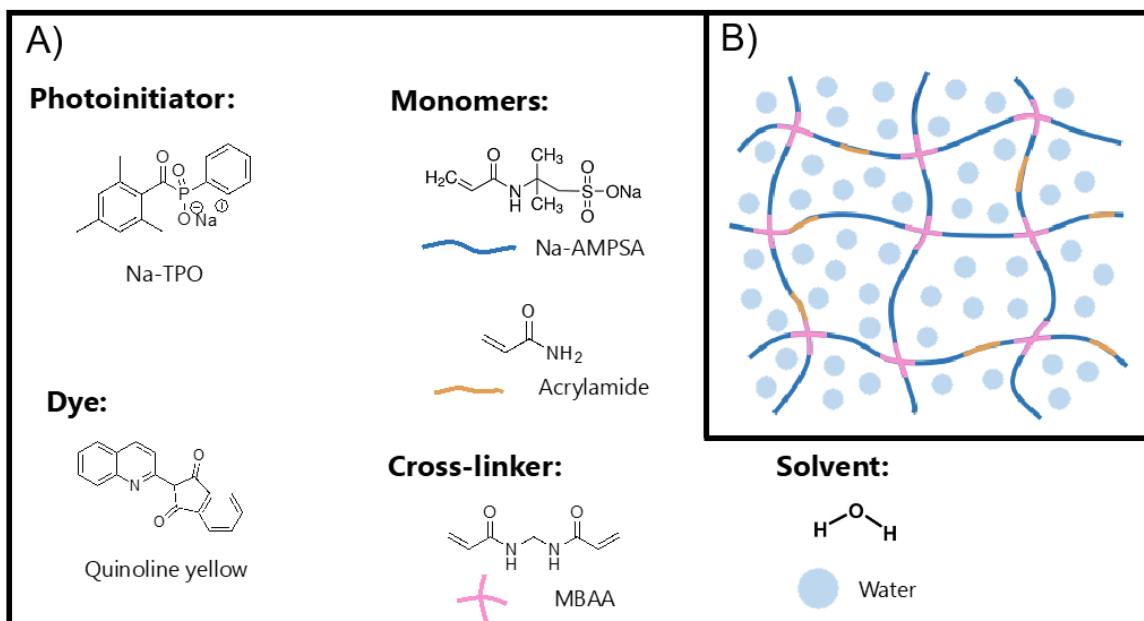
Figure 2.1. A) Chemical structures of resin constituents (photoinitiator, monomers, cross-linker and dye). B) An illustration of the hydrogel network.

II.2. Software

This section highlights the process of modeling the lattices, and the logic behind the methods used.

Before an object can be 3D printed, it must first be created with a computer-aided design (CAD) program and then converted into instructional code for the 3D printer. Rhino 3D and the integrated graphical algorithm editor, Grasshopper, were used to make the 3D models, and Cura was used as the slicing program to divide the 3D model into printable 2D slices.

The lattices begin as a collection of lines that make up the unit cell (**Figure 2.2)**. The Rhino environment was utilized to make the units cells of the lattices, as it emulates how one would draw on paper, but in 3D space, while still providing precision. Lines can be snapped into incremented angles and lengths, which is ideal for making objects of symmetric, repeated geometries. If it were to be done with Grasshopper, the 3D space would first have to be defined, and the start- and endpoints of the lines would have to be described with coordinates within that space; something that becomes increasingly difficult as the nodes of the unit cell deviate from simple factors of the principal planes' dimensions. The individual unit cells were created on separate layers within Rhino. Those layers were then referenced in Grasshopper, where they could be modified without influencing the original unit cell in Rhino. Once in Grasshopper, the unit cells could be arrayed into an n^3 lattice. The lattices at this point are only lines. This is intentional as it uses less computational resources, which is important when working

with a lattice of hundreds of elements that increase exponentially with n. When the lattice is arrayed to the desired n, a built-in piping algorithm is applied, which applies a cylindrical surface along the length of each line and caps the ends with spheres, resulting in a lattice of cylindrical beams (**Figure 2.3)**. The completed models are then exported as an STL file to the slicer program.
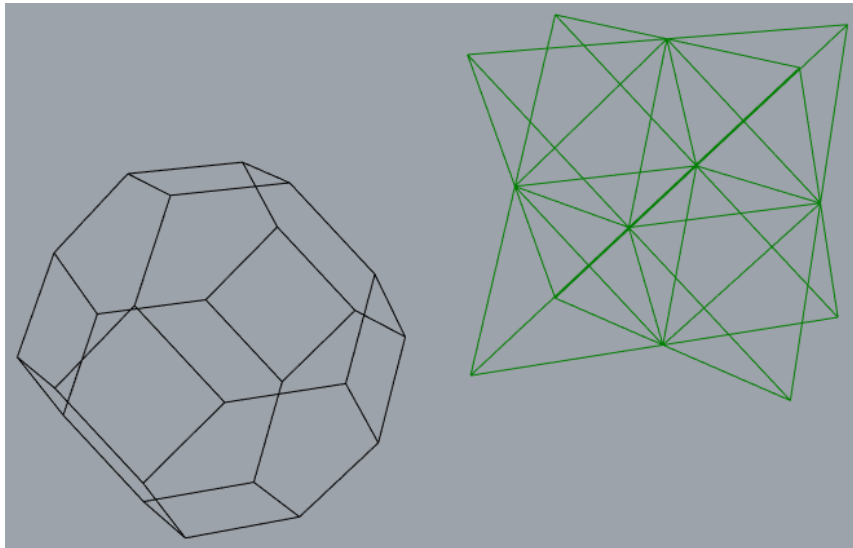

Figure 2.2. Unit cells of (left) truncated octahedron and (right) octet drawn in Rhino 3D.
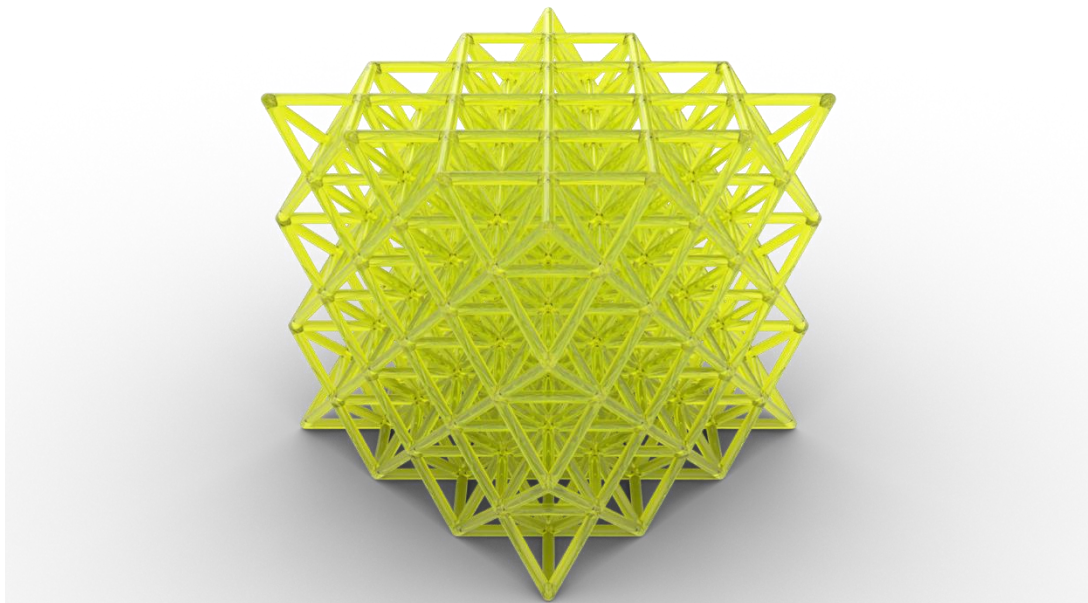

Figure 2.3. Final octet lattice created in Grasshopper, rendered in Rhino to look like a freshly printed gel.

Note: Although it is possible to create and modify the lattices entirely in Rhino, Grasshopper has the ability to adjust the extent of the lattice and the beam diameters with a click of a button. On Rhino, several steps would have to be made to change the beam diameter and the array would have to be performed with each change of the unit cell's dimension.

The function of the slicer program is to convert the 3D model into a set of instructions that can be performed by the 3D printer. The visual representation is a succession of 2-dimensional layers of raster patterns (**Figure 2.4**). The patterns represent the pathway the laser will take during printing. The thickness of the layers, the pattern and its density, and the width and speed of the raster line are some of the parameters that can be controlled with the slicer program. After the settings are configured, the program outputs a G-code file, which is the instructional code for the 3D printer, and the model can then be printed.
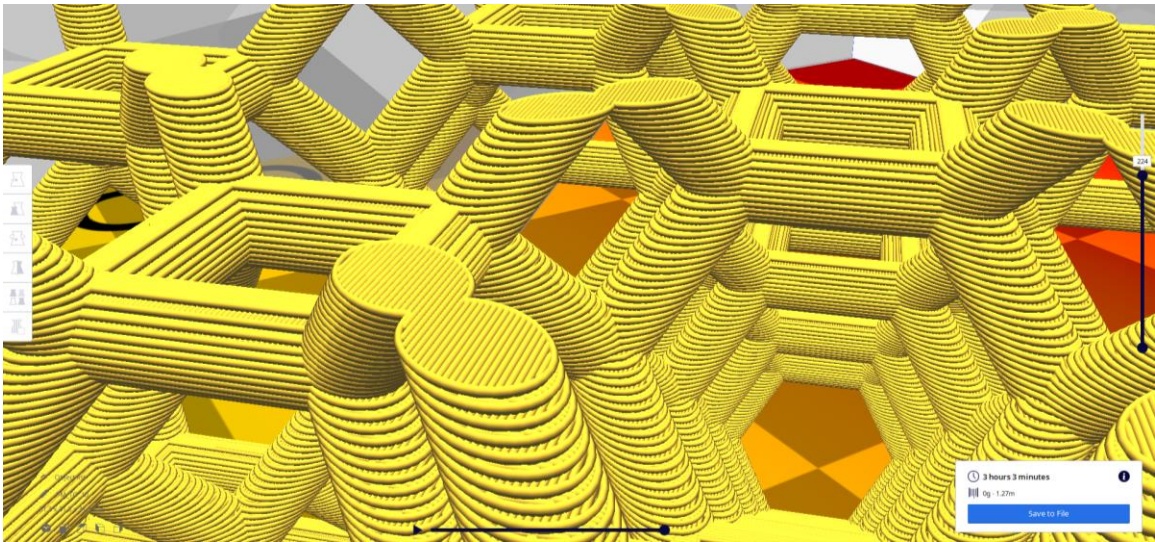

Figure 2.4. Slices and raster pattern of a truncated octahedron made by the slicer program (Cura).

II.3. Modification of a Commercial 3D Printer

A commercial SLA printer, Peopoly Moai, was chosen due to its open-source software, tunable printing parameters (print speed and laser power) and modification-friendly components. The Moai utilizes a near-UV (λ = 405 nm), 150 mW laser, and can achieve a 5- micron step height and 70- micron lateral resolution. Specifications can be found on their website: https://peopoly.net/collections/frontpage/products/moai-130-sla-printer-kit-version

II.3.1. Custom Resin Tank

The Moai came equipped with a 1-liter resin tank and 169 cm^2 build plate. The original resin tank's capacity was too great for resin prototyping and was immediately replaced by a smaller, fabricated tank (**Figure 2.5**). The replacement tank enabled low-volume printing (~20 mL), which greatly reduced material consumption during initial resin prototyping and during fouled PDMS replacement.
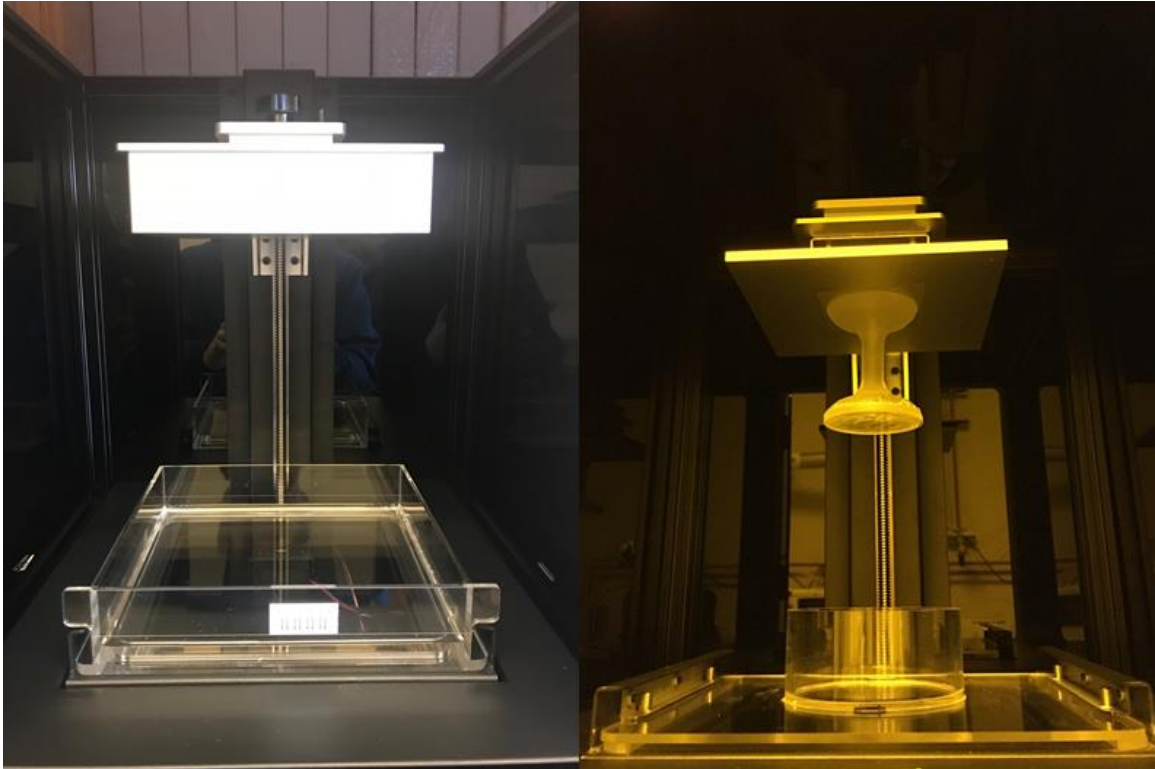

Figure 2.5. Original build plate and resin tank (left) and custom-made build plate extension and version 2 resin tank (right).

The custom resin tank was designed to be simple and modular to reduce fabrication time and allow for several iterations with a range of capacities if needed. It consisted of a 7/32" thick cast acrylic sheet and 3.25"/ 3" outer diameter/ inner diameter circular tube mated with cyanoacrylate super glue. The sheet was cut down to the dimensions required to fit it securely into the guide rails of the 3D printer's tilt platform (**Figure 2.6**). The circular tube was also cut to provide the desired volume when filled about halfway with resin. Increasing the capacity of the resin tank was as simple as attaching a larger circular tube to another acrylic sheet.
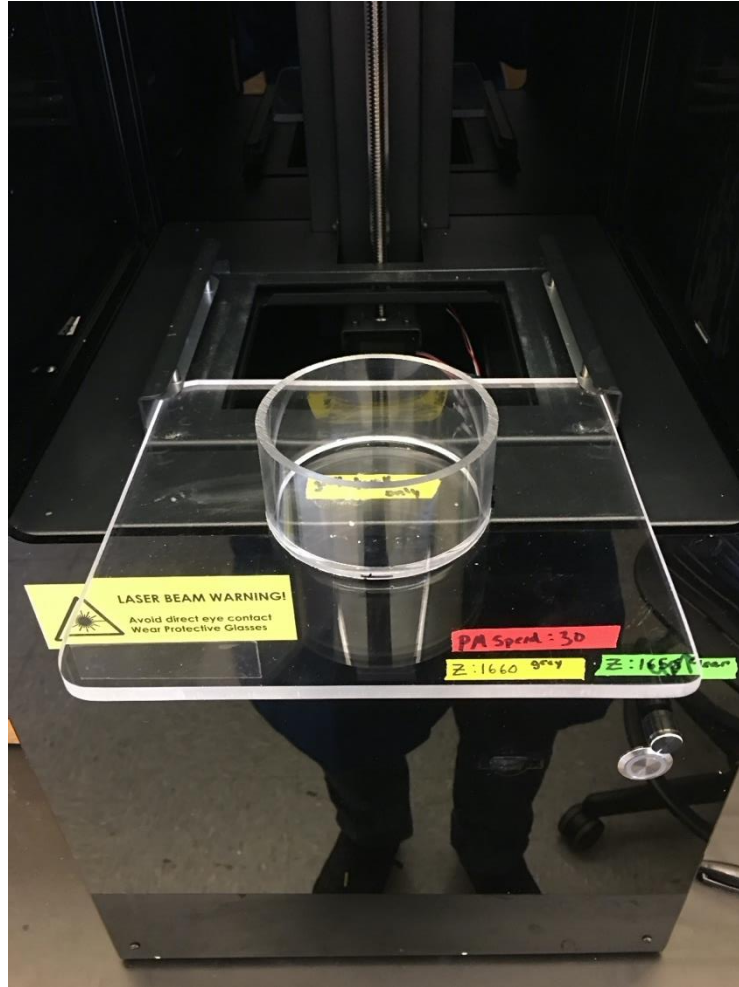
Figure 2.6. Version one of the custom resin tank partially placed in the guiderails of the Moai's tilt platform.

Two versions of the custom tank were made due to a design flaw with version one. Version one utilized a single sheet of acrylic to achieve a secure fit into the tilt platform's guide rails. Over time, scratches began to show on the bottom side of the acrylic sheet, as it was rubbing on the metal tilt platform each time it was inserted and removed. The scratches scattered light from the laser, leaving their resemblance on the printed gels. To address this, a sheet of acrylic that was half as thick (7/64") as version one was made, and pieces cut from the same sheet were glued to the bottom where the resin tank interfaces with the guide rail. This allowed the resin tank to maintain its secure fit, while also creating a gap between the area of the sheet that is exposed to the laser and the tilt platform. This was the second and final version of the resin tank.

An added benefit of the custom resin tank was the reduction of PMDS use. The resin tank has a PDMS layer on the bottom of the inside of the tank. Its purpose is to create a surface that discourages the print from adhering to it, so the print adheres to the

previous layer instead. Over time, repeated exposure to the laser fouls the PDMS, requiring it to be replaced. The replacement period depends on the laser settings and frequency of printing, but when initial resin prototyping was being performed, the PDMS layer was being replaced once or twice per month. The custom resin tank required 8X less PDMS than the original resin tank.

II.3.2. 3D-printed Build Plate Extension

The original build plate was too large to fit into the smaller tank, so an attachment was employed as a narrow extension of the existing (Moai's "easy-to-level") build plate, followed by a glass disk on which the gels were printed.

The initial version of the build plate attachment was made of Polylactic acid (PLA) and manufactured using an FDM printer (**Figure 2.7)**. However, over time the layers delaminated, causing resin to infiltrate the hollow body of the attachment during printing. This meant that resin was being removed from the resin tank each time a print was made (about 3 mL/print). The delamination might have been a result of the acidic nature of the resin etching away at the layer interfaces; and possibly excess stress at the interfaces from the leveling process, which involved pressing the build plate into the PDMS layer for contact leveling, and sometimes resulting in a violent separation at the glass build plate-PDMS interface. The final version of the build plate attachment was made with a Form Labs 2 using their Clear v4 resin. All issues pertaining to the PLA attachment were resolved upon implementation of the poly (methyl methacrylate) print. This is due to the high degree of crosslinking and relatively non-existent layer-layer interface in comparison to the build plate attachment made of PLA.

The attachment had a unique shape resembling an hourglass, which was key to efficient printing (**Figure 2.8**). The narrow midsection allowed the extension to be placed into the resin tank while limiting the amount of displaced resin when the build plate and extension are submerged in the resin. This also permitted printing with large quantities of resin when desired. The sloped topside of the expanded lower section allowed resin to flow back into the resin tank when the build plate emerges from the resin surface. And finally, the wide ends allowed for a larger printing surface and mounting area. Double-sided tape was used to adhere the extension to the original build plate and to adhere a glass disk to the bottom of the extension. The glass disk served as the build plate where the hydrogel was directly printed.

Figure 2.7. First version of the build plate extension made of PLA by an FDM 3D printer. The cracks (highlighted by the arrow) that led to uptake of resin can be seen near the top. It should be noted that the cracks were only hairline when the issue was discovered and have gotten worse from the removal of the glass disk and adhesive. Notice, too, that the shape varies from the second version. The first version was made to directly attach to the elevator rather than act as an augment of the existing build plate.
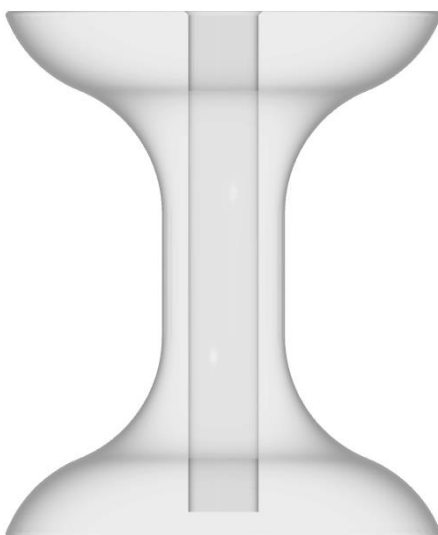
Figure 2.8. Transparent side view of custom extension. The cylinder running down the midsection is a cavity made to house magnets for future work.

II.4. Printing Process Development and Optimization

II.4.1. Printing Solids

Before the complex lattice structures could be realized, it was necessary to establish a baseline with solid structures. Developing the print process by first printing simple solids, like cylinders and cubes, allowed for the development of an intuition that would be handy when troubleshooting failures of lattice structures. For example, printing solids provided a simple way to measure exterior dimensions of prints, which provided insight into the build plate leveling procedure and how being off by only 100 microns could exclude print features or even lead to print failure. It also informed about the swelling that the gels undergo during printing, which was important in designing the experiment that led to the first successful print of a lattice.

II.4.2. Printing Lattices

Unfortunately, the printing parameters that were established for the simple solids did not directly carry over to printing lattice structures. The first attempts to print a lattice resulted in prints that had features of a lattice but were incomplete or had entirely fallen off during printing. It was thought at the time to be caused by a combination of shifting of the resin and the loading and unloading from buoyant forces when partially retracted from the resin during layer changes (**Figure 2.9**). To counter this, additional resin was added to the tank so that the gel would remain submerged for the entire duration of

printing. Keeping the gel submerged in resin eliminated the dynamic loading on the gel-build plate interface. Additionally, the resin acted as a support bath, which allowed for the printing of a lattice structure that was too soft for ambient conditions but may be useful for aqueous environments. To clarify, lattices could be printed with the solid parameters, but the gels exhibited low stiffness and would collapse due to surface tension of residual resin trapped within the unit cells. It may be possible to utilize such a material, as it becomes stiffer when swelled with water and may be able to retain its shape under ambient conditions, but it did not fit the scope of the research and was discarded. The next step was to increase the stiffness of the hydrogel.
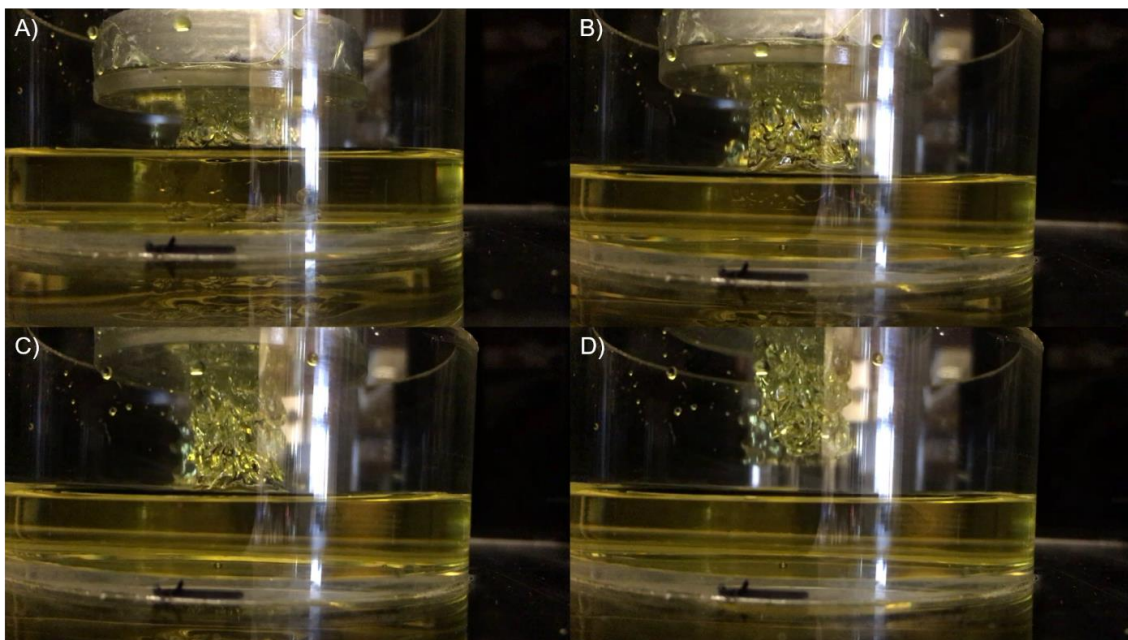

Figure 2.9. Inside of 3D printer during an early attempt to print a lattice that was ultimately too soft to resist surface tension of residual resin. The figure shows a series of frames depicting the extraction of a print after its last layer. A) How the hydrogel looks during printing when too soft and not completely submerged in the resin. The hydrogel has become detached from the build plate in some areas due to the residual resin pulling it inward. The lower portion of the gel that is submerged in the resin is fully supported by the hydrostatic forces acting in all directions. B, C) The hydrogel being extracted after the final layer is printed. The interface of the hydrogel and build plate has further deteriorated. D) The hydrogel is completely removed from the resin, and residual resin collapses the lattice.

The stiffness of the hydrogel is directly related to the degree of crosslinking; higher degree of crosslinking leads to higher stiffness. The print parameters that affect the crosslinking density are the print speed and laser power, as these ultimately control the number of photons interacting with the resin per unit of time. It is important to note that the laser power setting was near its upper limit when optimized for the solid prints. That is, if the power were increased further, the laser would start to degrade, leading to a

decrease of usable laser power. Therefore, the amount of water was reduced to increase the concentration of the resin and subsequently increase the reaction rate. This would allow for additional crosslinking at the same laser power. It should be noted that the print speed was not lowered any further, due to the increase in print duration. While this system is relatively quick in comparison to methyl methacrylate-based SLA, the print duration should be reduced as much as possible due to the swelling undergone by the hydrogel during printing. Too much swelling could lead to separation of the hydrogel from the build plate as a result of expansive forces overcoming the pinned initial layer. In this case, a reduction of print speed would also affect resolution, as too much exposure to the laser causes a sort of bleeding effect.

II.4.3. Resin-Print Speed Correlation

The first successfully printed lattice of adequate stiffness was the result of an experiment that simultaneously probed resin concentration and print speed. Since the failure of previous attempts was caused by the hydrogel's inability to support its own weight or resist the force of residual resin's surface tension, the parameters influencing the stiffness were investigated. Stiffness is a function of the degree of crosslinking, which is a function of exposure to the laser and number of reactive species. The degree of crosslinking can be increased by either increasing the number of reactive species per volume (through concentration) or by increasing the exposure to the laser (print speed). Therefore, an experiment was designed to qualitatively determine the best combination of concentration and print speed at a fixed laser power.

To track both resolution and stiffness simultaneously, a structure resembling a hybrid of a solid and wireframe cube was created (**Figure 2.10**). If stiffness were inadequate, the long and narrow beams of the wireframe would buckle due to the weight of the top frame, or they would warp due to shear loading during layer transition. If resolution were poor, the 2 x 2 mm hole would occlude due to overexposure to the laser.
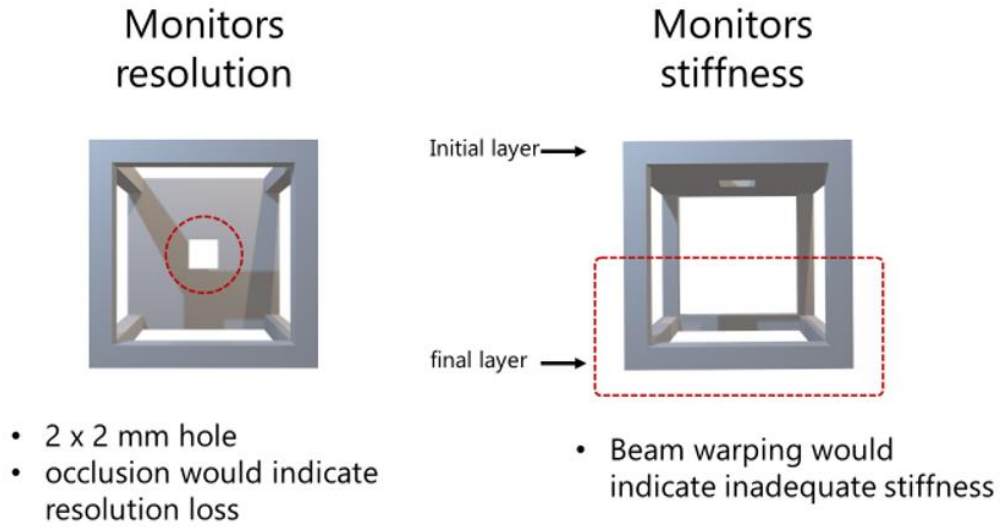
Monitors resolution

- 2 x 2 mm hole
- occlusion would indicate resolution loss

Monitors stiffness

Initial layer →

final layer →

- Beam warping would indicate inadequate stiffness

Figure 2.10. Hybrid wireframe cube used for monitoring print parameters to optimize stiffness and resolution.

It was believed that the warping resulted from the misalignment of the lattice's beams during layer transition. During the transition, the build plate is slightly retracted, and the resin tank tilts to delaminate the recent layer from the PDMS layer. When the build plate and resin tank return to their print position (resin tank flat, build plate 100 microns above PDMS surface), the laser begins the subsequent layer raster pattern. However, it was observed that the resin was still in motion from the tilting. It was believed that If the gel were not stiff enough to resist the motion of the resin, it would sway with it. So, the laser would begin the subsequent layer before the beams could return to their original position. The effect can be seen in **Figure 2.11**. This was never directly observed during printing, but other previous prints with long narrow features parallel to print direction exhibited similar warping in the direction of the tilting (**Figure 2.12**).
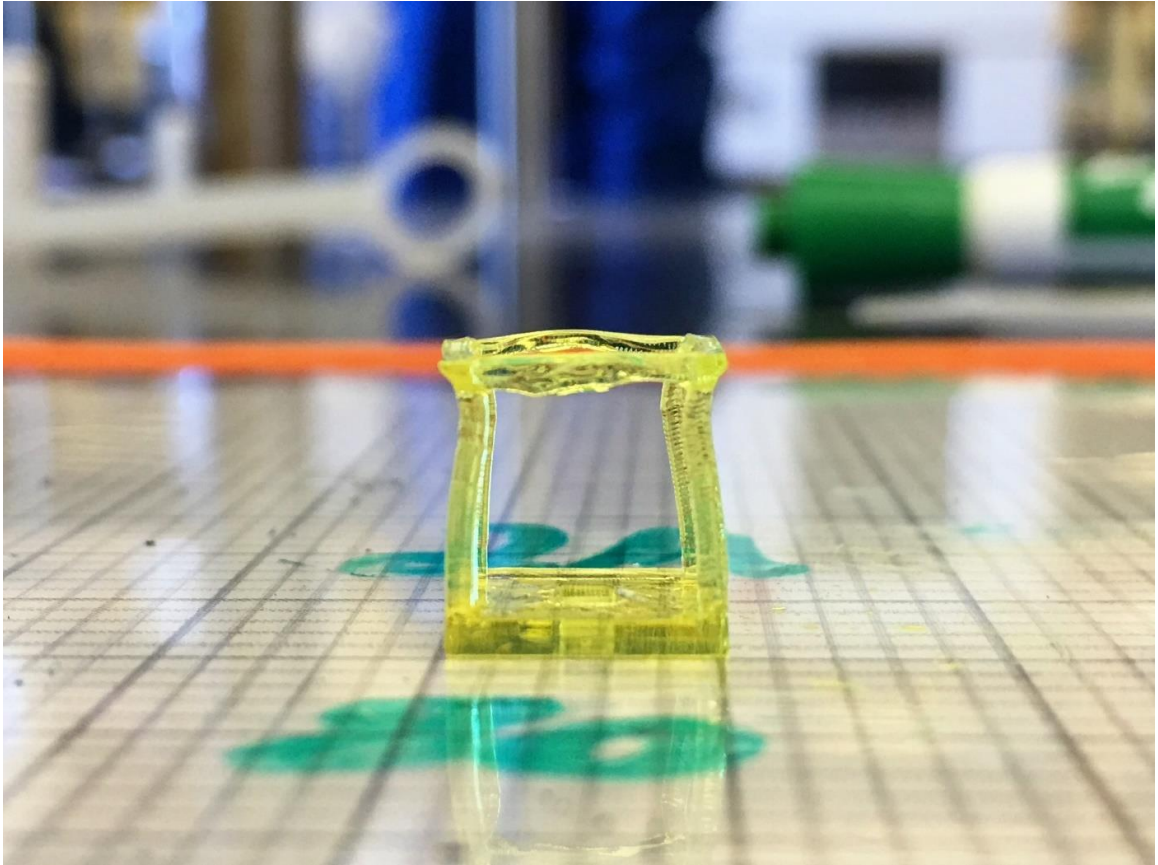
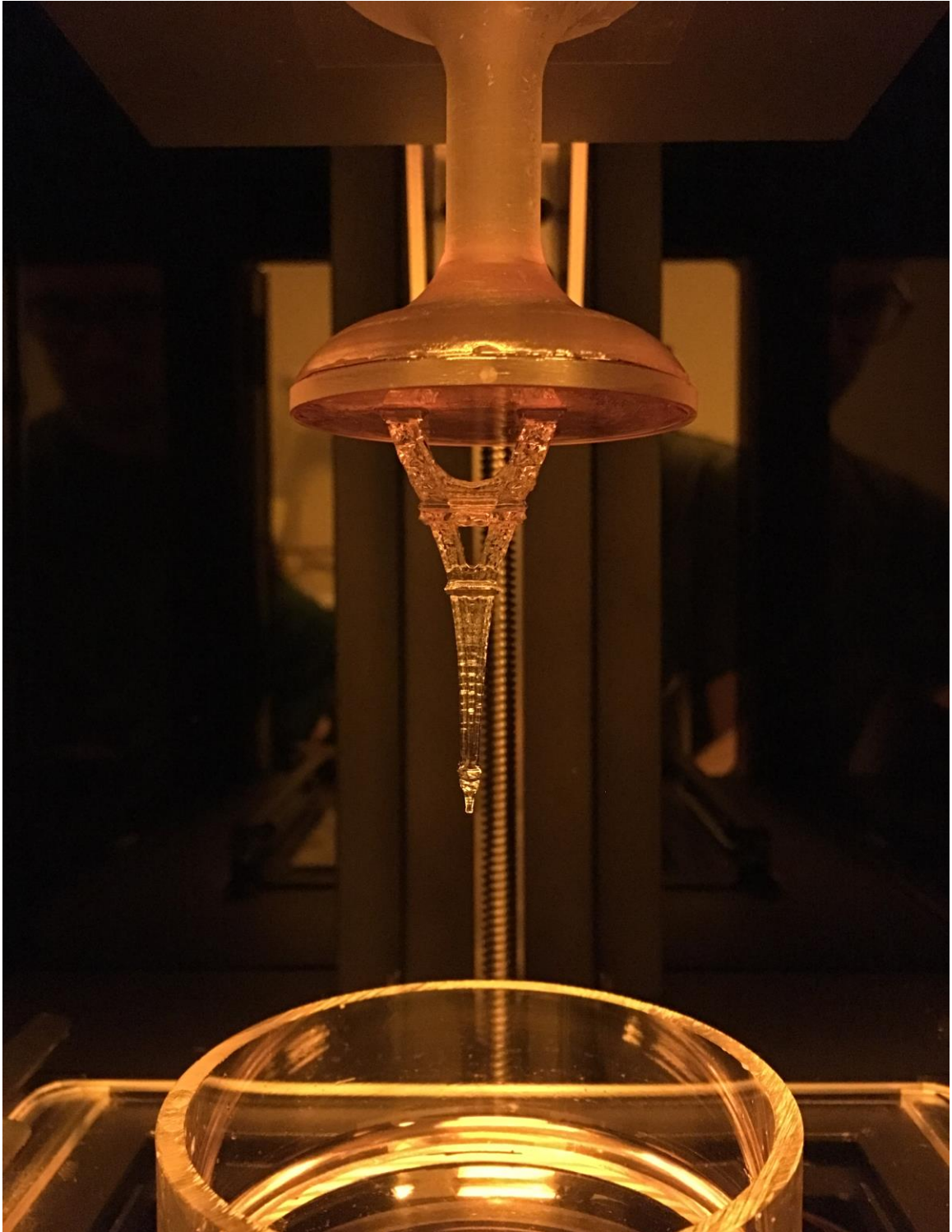**Figure 2.11**. Warping of features from inadequate stiffness.

Figure 2.12. An example of warping that occurs in the tilt direction.

A resin of double and triple the concentration of the original was used to print the hybrid cube at a gradually decreasing print speed. Starting from the rate used for solids (80 mm/s), the print speed was halved for each successive print until the hole occluded, and beyond for the sake of knowing what happens when overexposure occurs (**Figure 2.13**). Prior to each print, the resin tank was filled to a level that would keep the build plate below the resin's surface for the entire print duration. As mentioned previously, this was to limit the shear forces on the hydrogel-build plate interface, and to use the resin as a support bath. When the print was complete, the build plate was removed, and the hydrogel was patted with a paper towel to remove residual resin. The build plate with the hydrogel still attached was placed on its side so that the build plate surface was orthogonal to the tabletop. An initial impression of the stiffness could be gathered by observing the amount of bending the hydrogel underwent in the initial to final layer direction (**Figure 2.14**). While this method certainly has its application, the alignment of the camera and build plate added a degree of complexity and uncertainty for any collection of quantitative information. The hydrogel was then removed from the build plate using a razor blade and overlaid onto a grid. The grid consisted of larger and smaller cells matching the outer and inner dimension of the hybrid cube (**Figure 2.15**). The grid allowed for direct observation of any occlusion and bleeding.
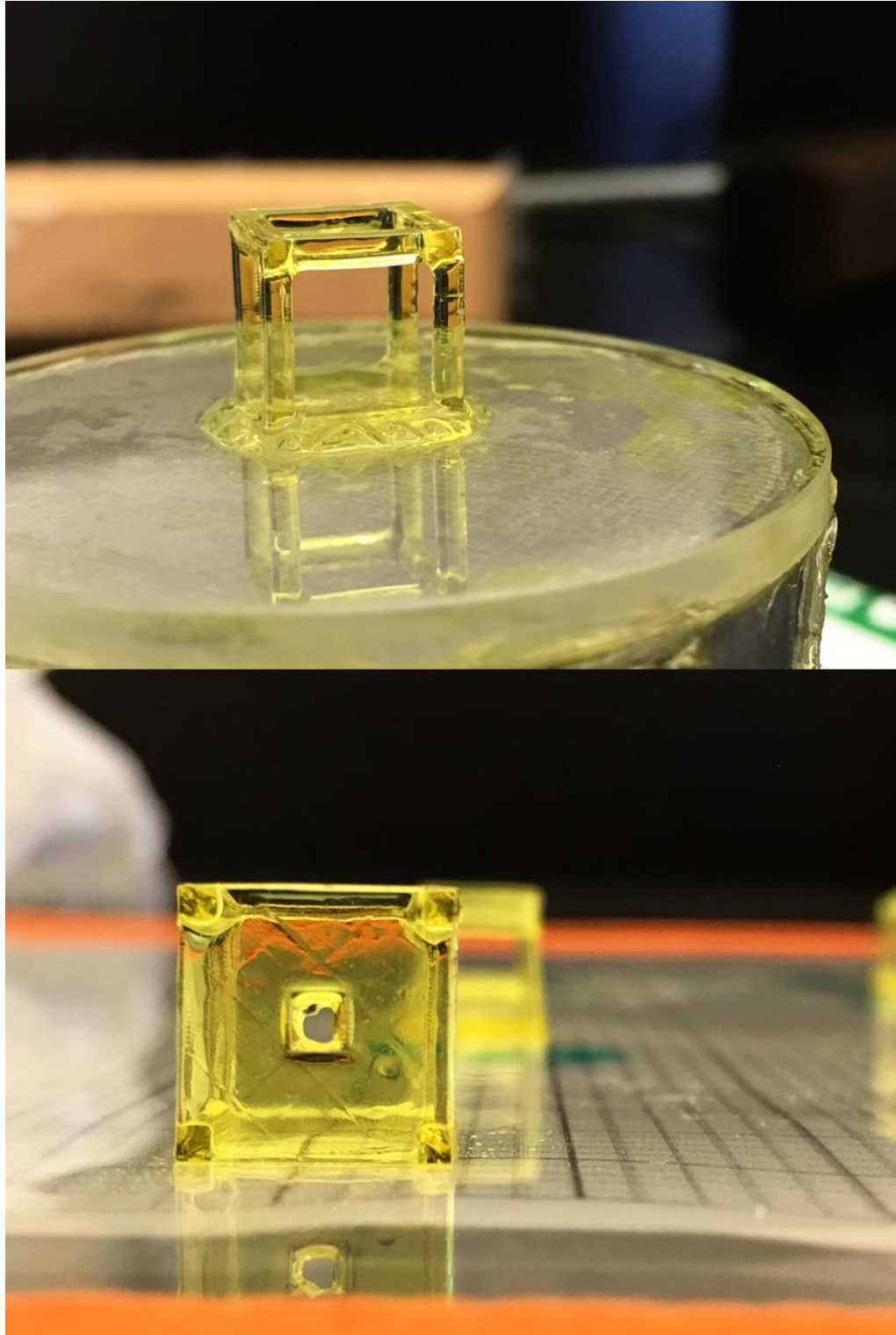
Figure 2.13. Examples of overexposure to the laser. Occlusion occurs, resulting in the loss of fine features.
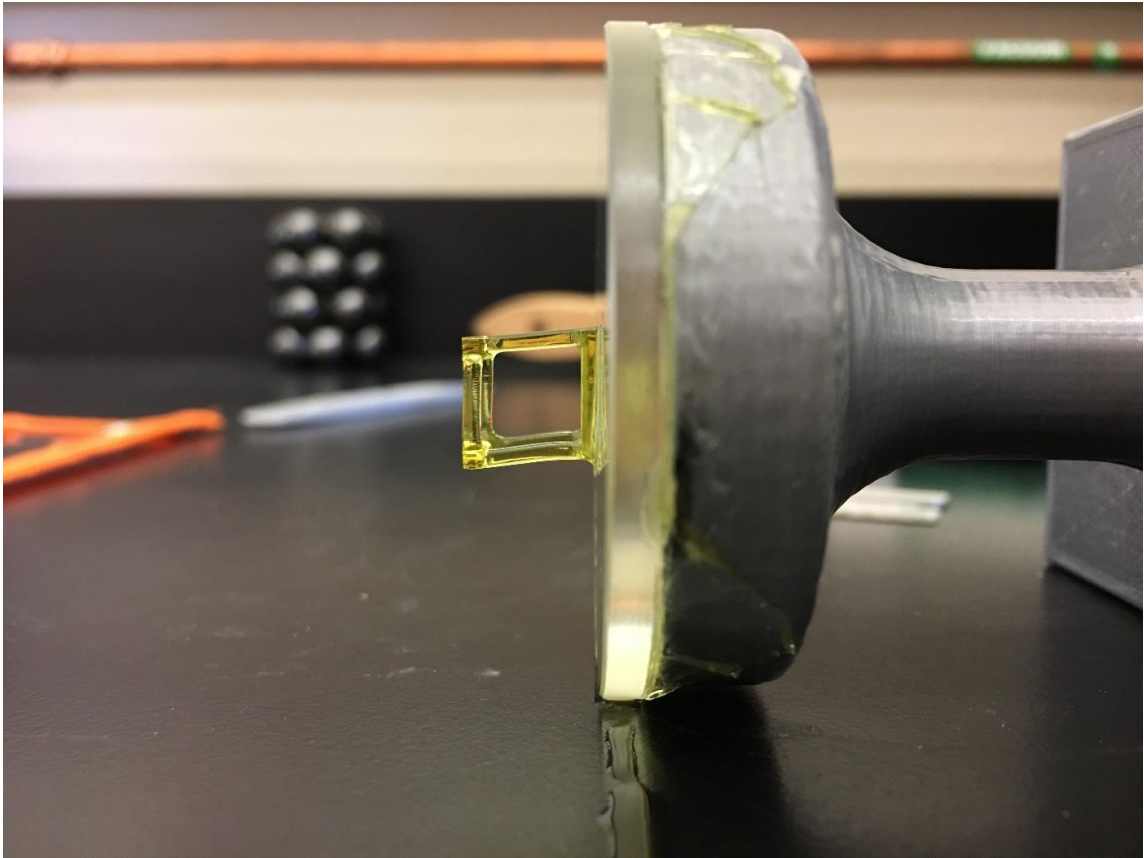
Figure 2.14. Hybrid wireframe attached to build plate extension. Can be used to gather impression of stiffness by observing the bending along the print direction.
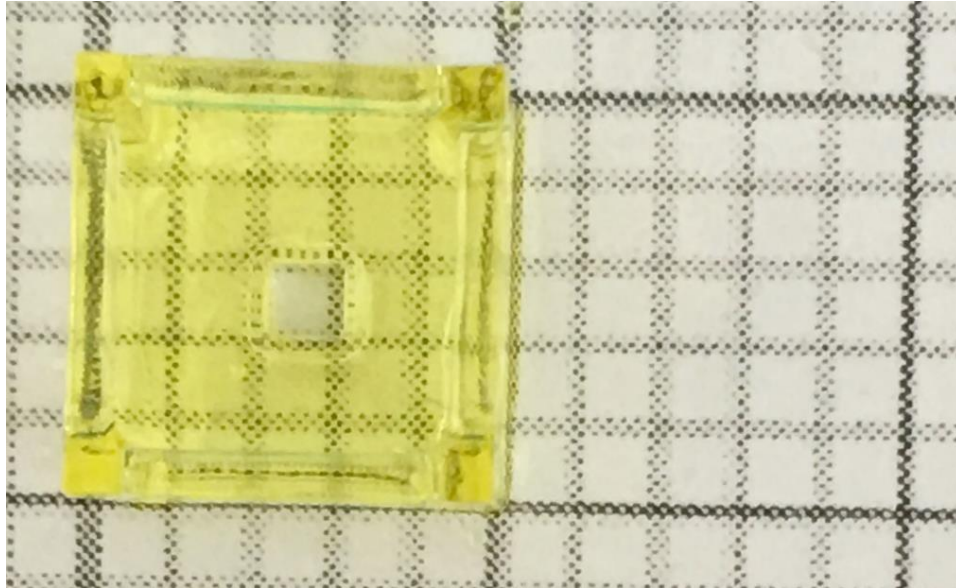
Figure 2.15. Hydrogel atop a grid being used to track print dimension. Larger grid is 10 x 10 mm, smaller grid is 2 x 2 mm.

For brevity, the following format of *2X.80* will be used to identify the resin concentration and print speed with a single term, where the item to the left of the decimal represents the concentration of the resin (2X or 3X), and the item to the right of the decimal represents the numerical value of the print speed in millimeters per second. As can be seen in **Figure 2.16A**, the initial result of 2X.80 was a print of adequate resolution but inadequate stiffness. 2X.40 (**Figure 2.16B**) had adequate stiffness and resolution, but the experiment was continued for insight into the behavior of the system when conditions lead to overexposure, as it would be formative to the intuition previously mentioned. Beyond 2X.40 the hole occludes, indicating overexposure, something that cannot happen when printing complex structures with fine features.
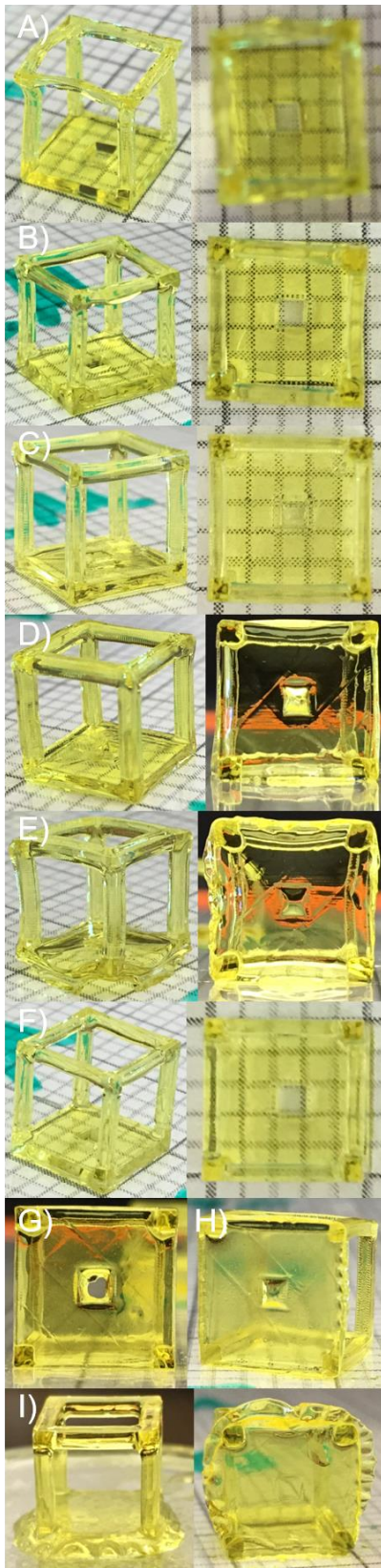
Figure 2.16. Pictures showing the relationship between resin concentration, printing speed, stiffness and resolution. For the sample labeling below, the first set represents concentration compared to the initial resin concentration (e.g. 2X means it is twice as concentrated), and the second set represents printing speed (e.g. 80 means structure printed at 80 mm/s). A) 2X.80. B) 2X.40. C) 2X.20. D) 2X.10. E) 2X.5. F) 3X.80. G) 3X.40. H) 3X.20. I) 3X.10. Scale: larger grid is 10 mm x 10 mm, smaller grid is 2 mm x 2 mm.

While the step from 40 mm/s to 20 mm/s may seem large and could exclude useful parameters, the goal was first to perform a wide sweep and then narrow down if necessary. However, 40 mm/s was already at the bottom limit of a desirable print speed. And 3X.80 (**Figure 2.16F**) provided the same print quality in half the time, so it was not desired to probe the range of 2X.40-2X.80. Thus, 3X.80 was the concentration and print speed selected to continue.

3X.80 led to the first successfully printed lattice, as seen in **Figure 2.17**. In its current state, the system routinely prints complex lattices at 100 mm/s at lower laser powers. Certainly, the printing could take place at a more rapid rate, but the current settings were determined by a subjective measure of stiffness that would allow the lattices to better survive the handling of post-print processing.
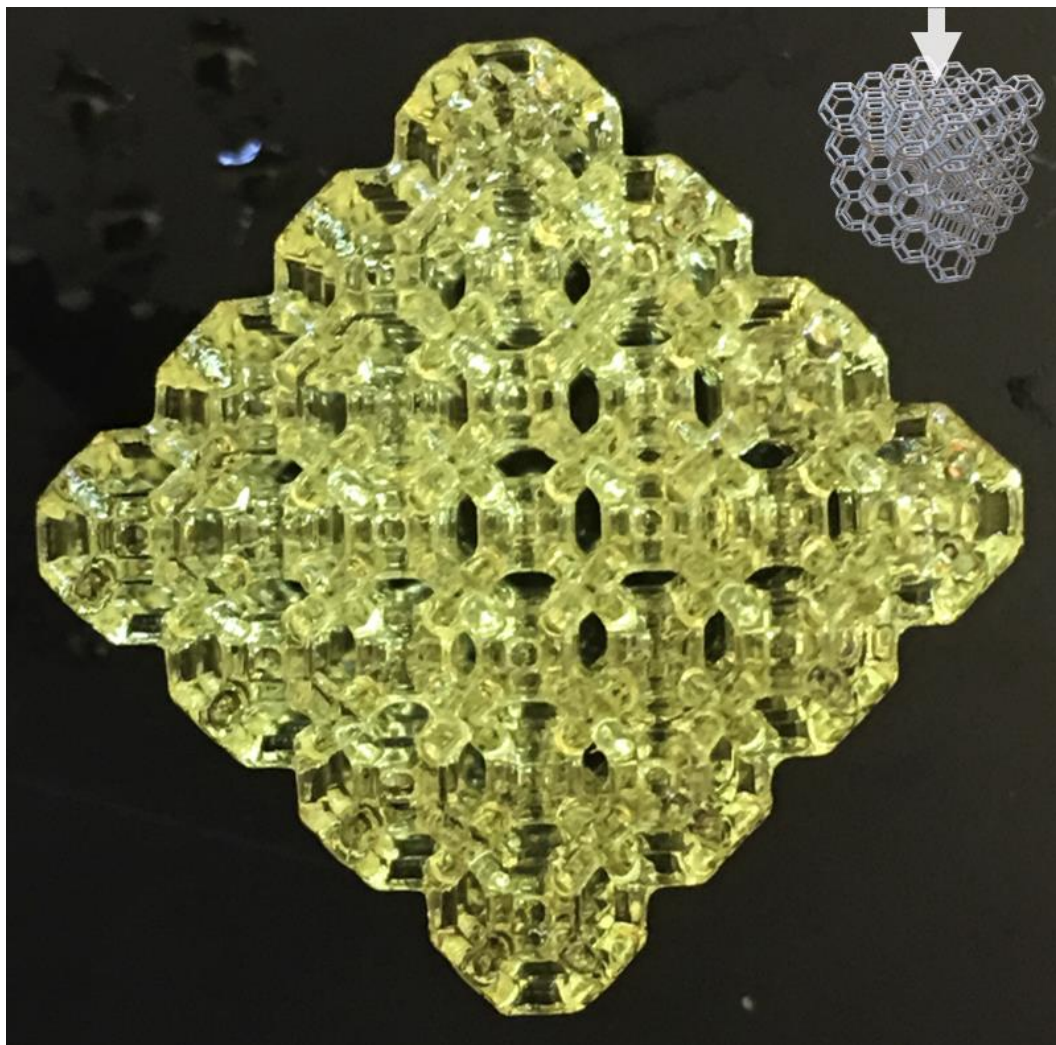

Figure 2.17. The first successfully printed lattice (4x4x4 truncated octahedron view from above).

II.4.4. Conductive Polymer Growth

The prints form a PAMPSA and polyacrylamide copolymer hydrogel in a partially hydrated state. The hydrogel plays both the role of a structural element and a doping polymer to the polyaniline. However, the prints only form half of the conducting polymer and need to undergo a post-print process to grow the conducting polymer (**Figure 2.17**). The aniline was polymerized by interfacial polymerization like the procedure described by Wu et al..[1] After removing the print from the 3D printer, it is placed into a bath of deionized (D.I.) water until the gel loses its yellow hue and becomes clear. The D.I. water serves to remove the dye and any unreacted species that remain inside the partially swollen gel. The amount of time will vary depending on the surface area-to-volume ratio of the printed object (1 – 16 hours). For example, the solid samples would be left overnight, but the lattices could be cleared in an hour if water is frequently replaced. Once the gel is clear, it is placed into a solution of 1 M HCl and 0.08 M ammonium persulfate (APS) for 1 – 16 hours. This step loads the gel with the required chemical species to carry out polymerization of the aniline. Next, the gel is removed from the solution and rinsed with hexanes, which washes off any residual solution on the surface or in the pores without removing the contents of the gel. Once rinsed, the gel is placed into a solution of 0.16 M aniline in hexane for 4 hours (**Figure 2.17**). After the growth of polyaniline, the conductive gel is placed into another D.I. water bath, to remove any unreacted species once again, for 1 – 16 hours. Then the conductive gel is placed in a 1M HCl solution for doping for 1 – 16 hours. And finally, the gel is placed into another DI water bath for 1 – 16 hours. **Figure 2.18** shows the gel at various stages of the process.
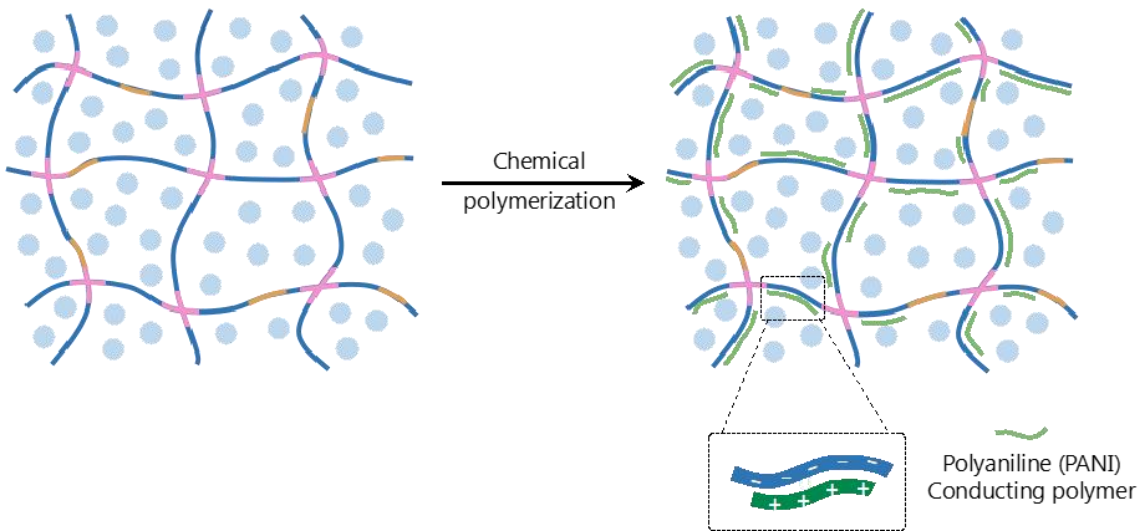
Figure 2.17. Truncated octahedron and octet lattices undergoing interfacial polymerization step. Left) Gels are swelled with HCl/APS solution and separated. Right) Gels in hexanes/aniline solution after interfacial polymerization of polyaniline has occurred.
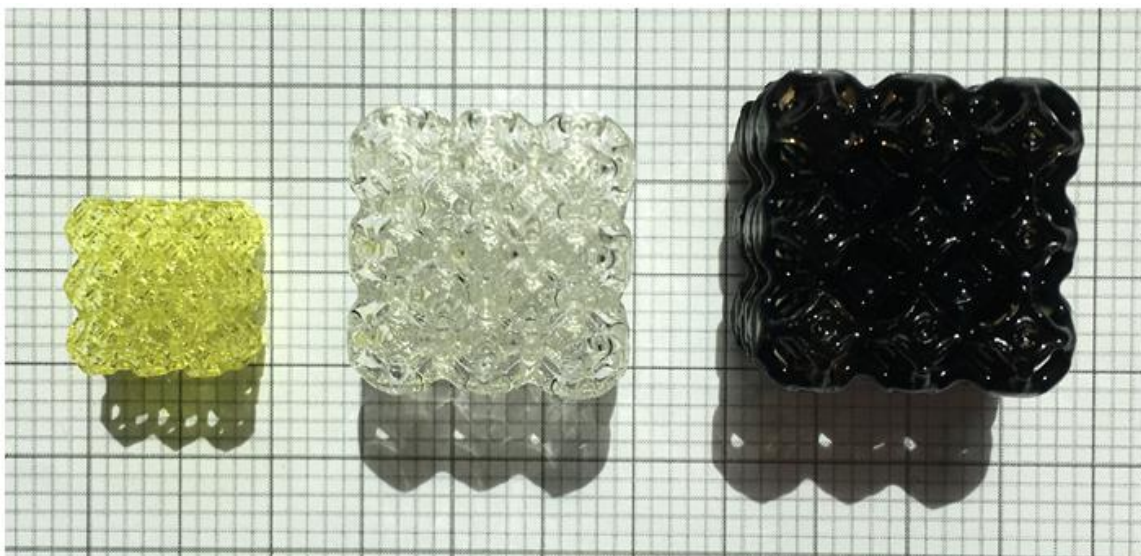
Figure 2.18. Hydrogel at various stages of the post print-process (post-print, rinsed and swelled, and with polyaniline). Larger grid is 10 x 10 mm, smaller grid is 2 x 2 mm.

References

1. Y. Wu, Y. X. Chen, J. Yan, S. Yang, P. Dong, P. Soman, *J. Mater. Chem. B* **2015**, *3, 5352.*

III. Properties of Hydrogel Lattices

This chapter introduces preliminary results of the mechanical and electrical properties of hydrogels and offers pathways to optimization.

III.1. Mechanical Behavior of Electrically Conducting Hydrogels

III.1.1. Solid vs. Lattice

After establishing a 3D printing system capable of reliably printing conducting polymer-based hydrogels into complex structures, the focus was shifted to characterizing the mechanical behavior of the bulk and lattice material. The first data collected was a comparison of the compressive behavior of a solid puck and octet lattice. An octet lattice of 20% relative density (relative density is explained in III.1.4.) was chosen to represent a lattice material.

Figure 3.1 shows the compression stress-strain curves generated by the solid and lattice electrically conducting hydrogels. The samples were to be compressed until reaching 80% strain or failure. The solid hydrogel compressed little beyond 25% strain before undergoing brittle fracture. However, the lattice hydrogel was able to compress beyond 60% strain without brittle fracture and exhibits a stress-strain curve with three distinct regions (**Figure 3.2)**, a characteristic of lattice materials.[1] While the test was more qualitative in nature, the result confirmed the viability of tuning the mechanical properties of a conducting polymer with architecture and prompted further investigation.
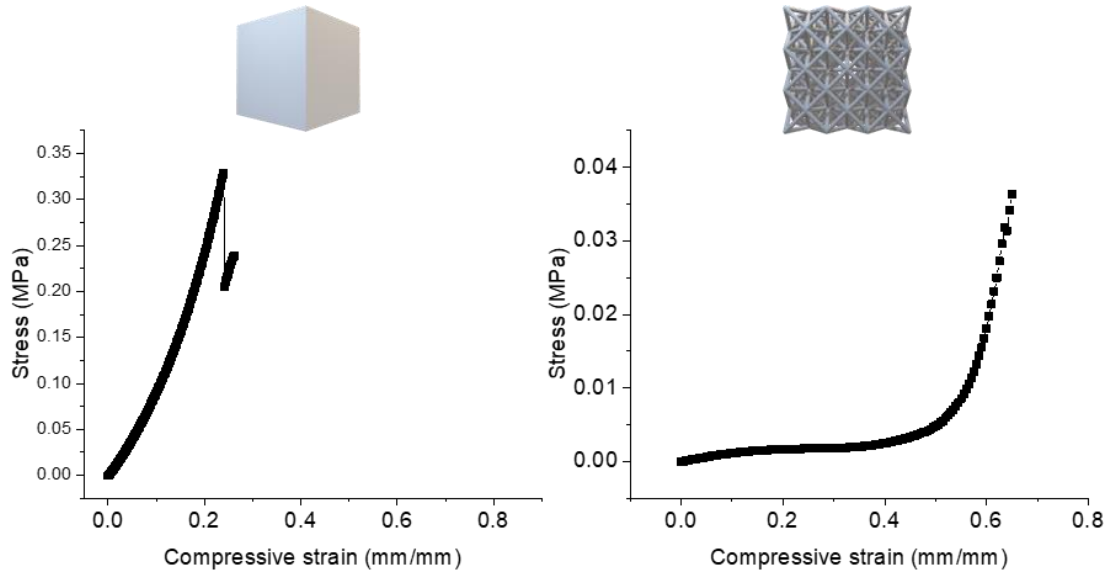
Figure 3.1. Stress-strain curves of solid (left) and octet lattice of 20% relative density (right).

Figure 3.2. The three distinct regions of the curve represent the following physical phenomena: A) the buckling of the lattice beams, B) the collapsing of unit cells, and C) the densification of the entire lattice. In the densification region, the mechanical behavior is no longer derived from the framework of beams but is instead derived from the compressing of the bulk material.[1]

III.1.2. Mechanical Property Scaling Behavior

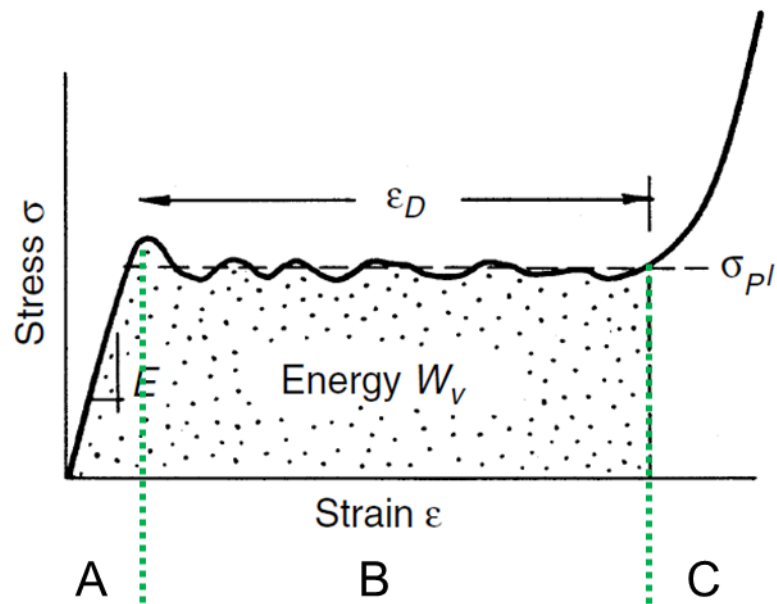During a materials selection process, classes of materials, or materials of the same class, are compared based on certain performance criteria using Ashby plots. Ashby plots are scatter plots that compare two or more desired material properties to develop a ratio between the properties (**Figure 3.3)**. This ratio is a performance metric and can be extrapolated via a straight line with the slope equal to the performance ratio. Any materials that intersect the line have the same performance. Ashby plots are routinely used to visualize and quantify lattice materials' expansion of property space of their constituent materials.[2] It has also been shown that the type of lattice, defined by its deformation mechanism, influences the rate at which certain properties deviate from the corresponding properties of bulk (fully dense) material. It is important to note that properties of the lattice material, such as strength, will be less than that of the bulk. However, the raw strength of the material is not the basis of performance, rather the ratio of strength to some other property, such as density. The importance of lattice materials is their ability to retain a significant portion of the bulk strength while reducing mass so that the property space can extend into regions that are empty. This effect is shown by the CFRP and aluminum lattice regions in **Figure 3.4**. It was of interest to investigate how the property space of lattice conductive polymers would behave, and if it would point to a definite way to tailor properties like stiffness and strength, or to modulate the three regions of the lattice material stress-strain curve. In an attempt to do so, lattices of a range of densities were compressed until failure. The goal was to track how the various properties scale with density.
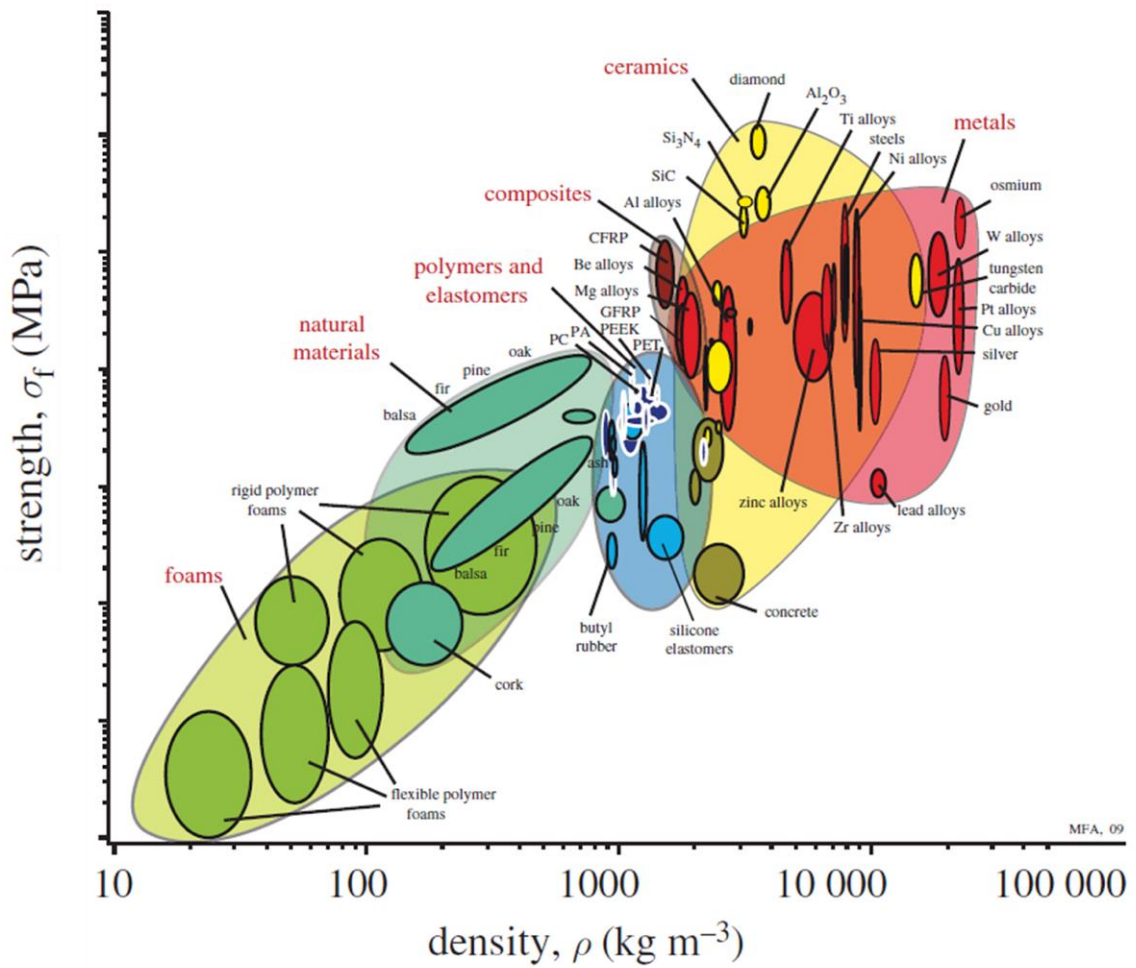
Figure 3.3. Ashby plot used for evaluating material performance for materials selection. (Adapted from ref. 2.)
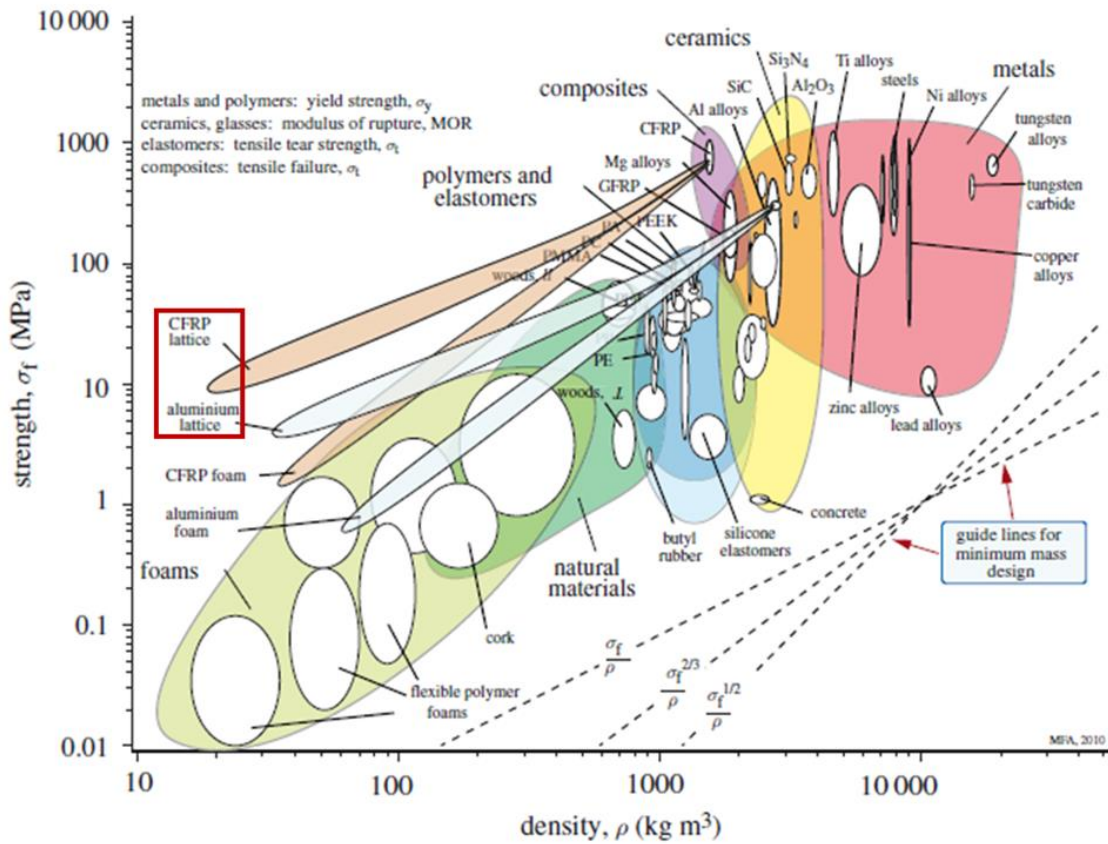
Figure 3.4. New property space enabled by lattice materials. (Adapted from ref. 2.)
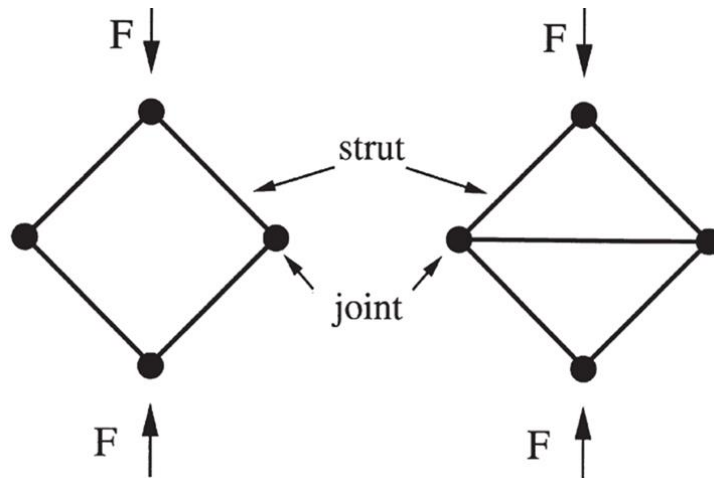

Figure 3.5. Simple pin-jointed frames illustrating bend and stretch structures.[5]

Lattice materials are characterized by the dominant deformation mechanism undergone by their constituent beams, which can be either bending- or stretching-dominated.[2] The beams of a bending-dominated structure primarily experience bending, and their properties depend on the bending stiffness and strength of the material. For stretching-dominated structures, the beams primarily experience axial compressive and tensile load, and their properties depend on the axial stiffness and strength of the material (**Figure 3.5**).[2] The truncated octahedron and octet lattice were chosen as they represent the two types of deformation mechanisms (bending- and stretching-dominated), and are common throughout literature.[3,4]

Initially, lattices of each type were printed with relative densities of 15-, 20-, 30-, 40-, and 50-percent and were compressed with a universal testing machine. The result can be seen in **Figure 3.6**, and the methods can be found in the later section: *Mechanical Test Setup (III.1.4)*. It was discovered after testing that there was an error in the calculated relative density. This is discussed further in the *Relative Densities Calculation (III.1.5)* section. In short, the densities of the truncated octahedron were half of what they were calculated to be and were not comparable to the octet samples. This data, while not able to serve its initial purpose of comparing the changes in mechanical properties of the two types of lattices, still can offer interesting information.
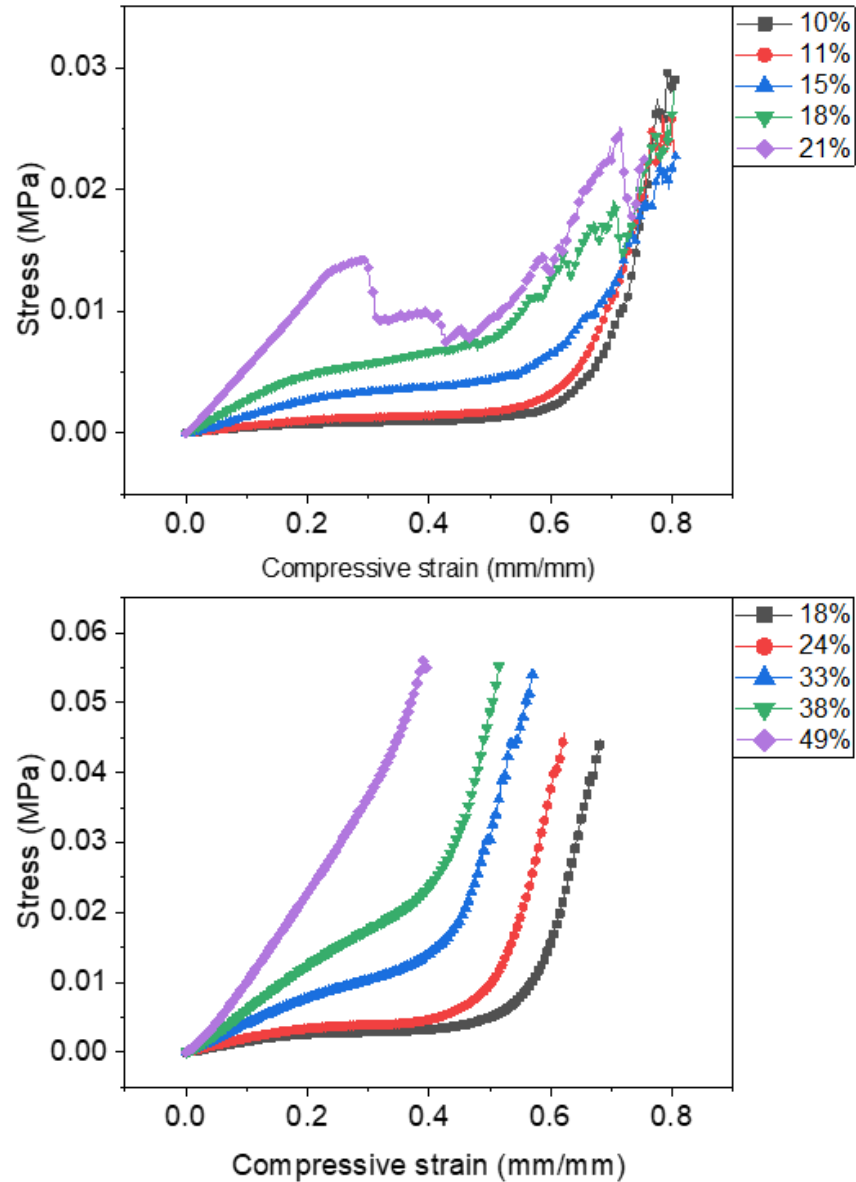
Figure 3.6. Stress-strain curves of the truncated octahedron (top) and octet (bottom) of various relative densities.

A noticeable feature is the diminishing of the plateau region as the relative densities increase. A closer look reveals that the truncated octahedron begins to rupture at a lower relative density than the octet. This is believed to be a result of how the volume fractions were calculated, rather than just a result of the different lattice types. When calculating the volume fractions, the outer dimensions of the unit cells were the same for each lattice type, and the diameter of the beams was used to modulate volume fraction.

However, the octet and truncated octahedron unit cells contain the same number of beams, but the beams of the truncated octahedron are half as long, which resulted in its beams having a larger diameter. It is hypothesized that, since the deformation mechanism of the truncated octahedron is bending, the larger diameter would decrease the aspect ratio of the beams to a point where loading is more likely to lead to failure at nodes than buckling of the beams; essentially diminishing the mechanism from which bending-dominated structures derive their behavior.

To address the aforementioned issue, the truncated octahedron and octet lattices should be made so that the beams of the unit cells have identical lengths.[3] This will, in turn, cause the beam diameters to also be identical. The *Relative Densities Calculation (III.1.4)* section discusses an issue related to beam diameter, which is believed to be a result of a resolution limit. Making the lattices with identical beams will reduce the number of variables when troubleshooting issues related to the printing process. However, this will also inevitably cause the truncated octahedron to be about twice as large as the octet. With the current setup of the 3D printer, printing lattices of that scale and of the quantity required to perform the analysis, will cause a massive increase in printing and processing time. It is highly recommended that the build plate and resin tank be made larger.

III.1.3. Strain Rate-invariant Stress Response

The lattice conducting polymer hydrogels were compressed at an increasing rate starting from 50%/min and ending at 1500%/min, which was the limit of the universal testing machine. As can be seen in **Figure 3.7**, there is negligible difference between the stress-strain curves. Typically, bulk materials will exhibit an increase in yield strength and a decrease in ultimate strain with increasing strain rate. This discovery led to the hypothesis that the electrical properties of the material would also exhibit a strain-rate invariance. This is discussed in the electrical behavior section.
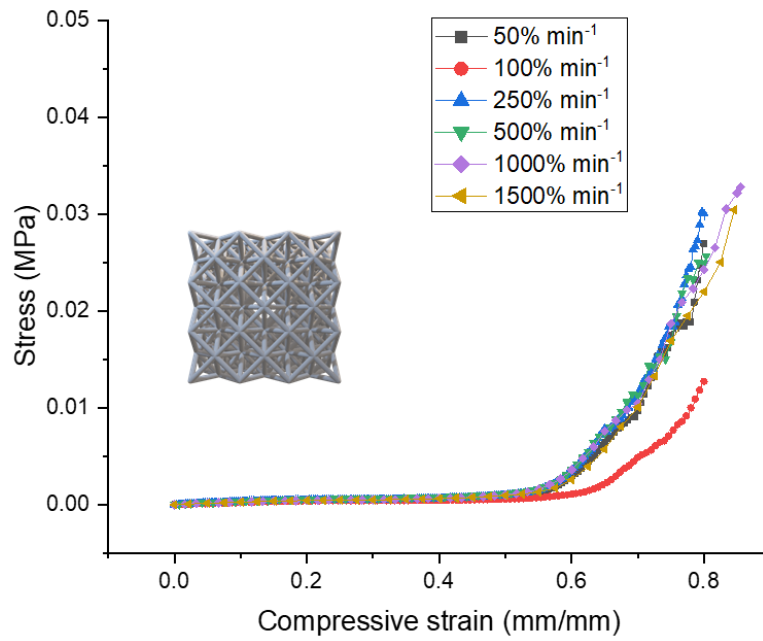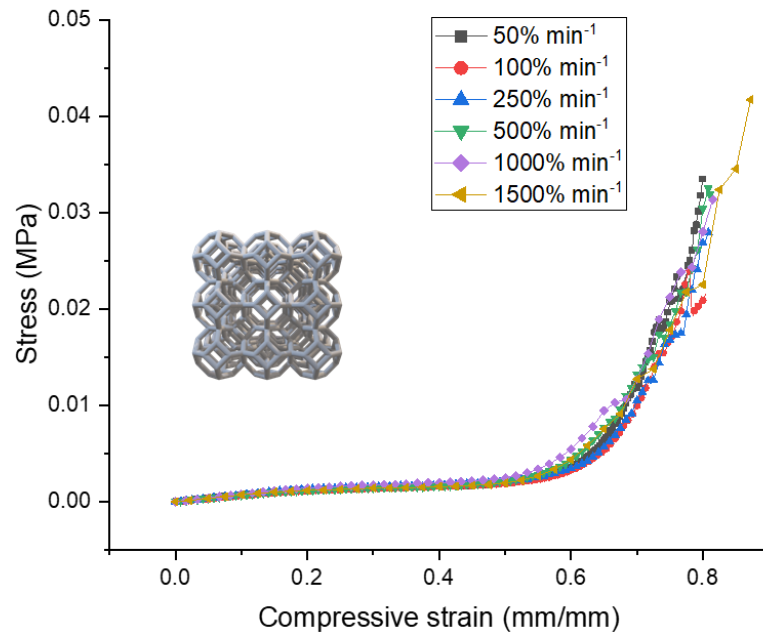
Figure 3.7. Stress-strain curves of various strain rates of an octet and truncated octahedron of 10% relative density. Responses are consistent over a large range of strain rate, minus the one outlier (OCT 100%), which will be repeated.

III.1.4. Relative Densities Calculation

The relative density of a lattice material is defined as the ratio of volume the lattice occupies to a solid of geometry that bounds the lattice (e.g., a cubic lattice within a solid cube of equal external dimensions).[2] The volumes of the lattices were calculated with Rhino 3D's volume calculation command. Volume was adjusted to the desired amount by changing the radius of the beam elements. The unit cells for each lattice type had equal external dimensions. Any changes in the external size of the lattice retained the volume ratio, as it was equally scaled in all directions.

Initial attempts to verify the calculated relative densities were made by measuring the mass and outer dimensions of fully hydrated lattice gels containing polyaniline and comparing them to a solid cube of identical condition. It was observed that water was being retained in the lattice cells, which created a degree of uncertainty of relative density calculations. In an attempt to remove the residual water, compressed air was gently blown into the cells in combination with padding a paper towel on the exterior. However, the hydrophilic nature of the gel caused the water to considerably wet the surface, resulting in an inaccessible film of water within the lattice. And given the high surface area of the lattice, it was assumed that the residual water was contributing to deviations in relative density calculations. To further elucidate, the mass of the solid cube, which has only six surfaces, deviated by 5 percent when subsequently dried with a paper towel after an initial drying. To address this, an experiment was done to determine if the gels maintained their density when dehydrated.

The same solid cube was placed onto a PTFE sheet and dried under ambient conditions. Ambient conditions were not recorded at the time. The PTFE sheet provided a low friction, hydrophobic substrate to reduce any pinning during dehydration. Once the gel appeared dry, the mass was recorded periodically to confirm the water had completely evaporated. Then the gel density was measured and compared to the wet density. The dry gel had a matching density of 1.1 g/cm^3.

Given the density results of the solid gels, it was assumed that the lattice gels would follow the same trend. Initially, the truncated octahedron and octet lattices were printed in 15-, 20-, 30-, 40-, and 50-percent volume fraction, as calculated by the CAD software. The measured relative densities of the octet (OCT) lattice were close to the calculated values, but the truncated octahedron (TO) relative densities were about half. It was discovered to be a result of the TO model not being a closed or solid object on the CAD program. When making these models in the CAD program, there is a function called "make solid", a common feature in most CAD programs that takes a collection of surfaces and makes them into one polysurface. While this feature is not necessary for making an STL, it was necessary due to it making the volume calculations easier to

perform. When the half as dense TO models were made, the make solid action was not performed, which was a user error. Most likely the volume calculation was being performed as though the beam elements were their own objects instead of one joined object, so the overlap between them was essentially being counted twice. During the correction of the calculated volume fraction, the cells of the truncated octahedron lattice began to close as the volume fraction approached 40%. It was decided that the range of volume fractions would be shifted to 10-, 15-, 20-, 25-, and 30-percent. The new lattices were then printed and dried. While most of the measured relative densities were within the margin of error (5%), some were beyond.

Further investigation showed a trend of increasing deviation from the calculated density (greater than) as a function of decreasing beam diameter. Comparing beam diameters to percent error displayed a shared behavior of greater than 5 percent error between the two lattices when beam diameter was less than about 800 microns (**Table 3.1**). It is hypothesized that the resolution of the printer is being reached, and that the deviation gets worse as beam size decreases. A possibility for this is the actual laser spot size is larger than the setting that the slicer program is using to calculate the laser path and infill, leading to overlap and a larger external dimension. This would explain why the densities trend towards higher values as the beams decrease in size. For a cylindrical beam, the portion of the laser that is outside of the cylinder's circumferential dimension is fixed and occupies a greater fraction of the cross-sectional area. This is illustrated in **Figure 3.8**.

Table 3.1. Relative density percent error greatly increases for both lattices when beam diameters are less than ~0.8 millimeters (gray)

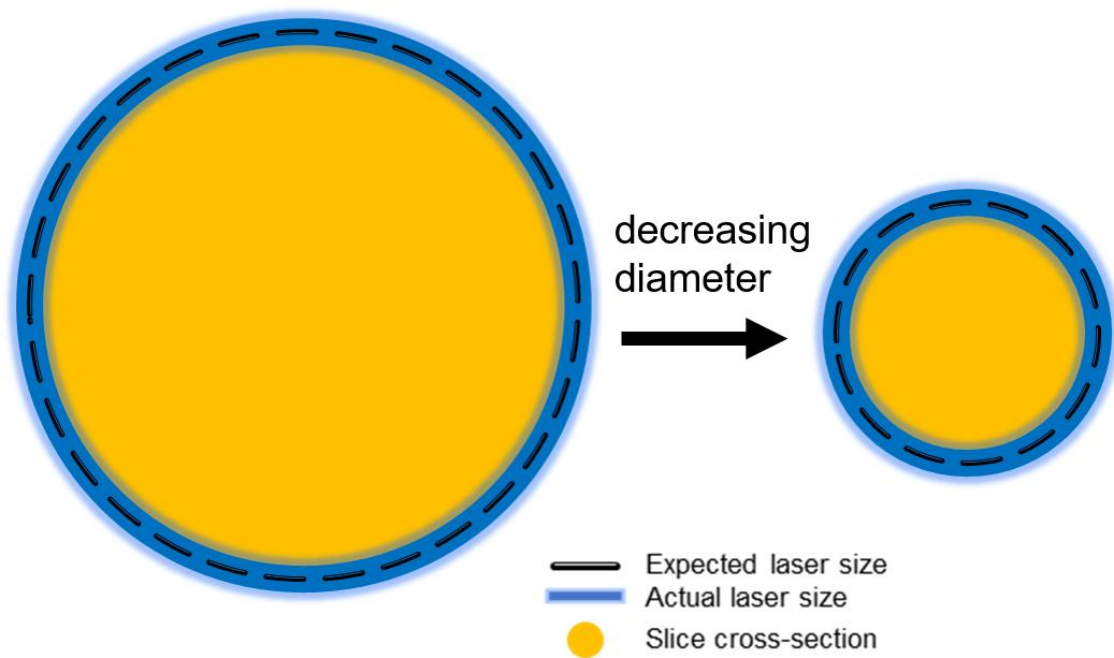|	Calculated relative density (ρ_L/ρ_s)	Measured relative density (ρ_L/ρ_s)	Percent error (%)	Calculated beam diameter (mm)
TO	0.10	0.14	39	0.699
	0.15	0.16	5	0.881
	0.20	0.21	3	1.037
	0.25	0.26	4	1.192
	0.30	0.31	4	1.335
OCT	0.10	0.16	63	0.488
	0.15	0.19	24	0.61
	0.20	0.23	14	0.718
	0.25	0.26	3	0.821
	0.30	0.29	2	0.915

Figure 3.8. Illustration of the proposed overlap and its greater area fraction for smaller diameter beams. The laser beam (blue) occupies a larger fraction of the cross-section (yellow) for smaller diameters.

It may also be possible that the overlap of the laser raster leads to a higher degree of crosslinking/polymerization, as the portion of the gel within the overlap is exposed twice, and there is certainly uncured resin within the gel to undergo further polymerization.

III.1.5. Mechanical Test Setup

A universal testing machine (Instron 3369) was used to characterize the compressive behavior and properties of the conducting hydrogel in their hydrated state. The machine was configured with compressive anvils and a load cell of 100 N. Samples were compressed to an ultimate strain of 80-percent at 100-percent strain per minute. Both ultimate strain and strain rate were determined by a series of tests that identified the limit to which a sample (of 20% relative density) could be compressed without failure, and the max rate the compression could be performed without noticeable deviations in the stress-strain curve.

Tests were performed under ambient conditions, as opposed to an environment that mimics the human body, since the goal is to address the mechanical properties of conductive polymers worn outside the body. Compression tests are performed in a matter of minutes and changes in hydration were not of concern.

As one could imagine, the hydrated gels are nearly frictionless and require extra effort to prevent them from being squeezed out from between the anvils during compression. A simple solution is to place a tissue paper between the anvil surface and gel. The tissue paper resists any lateral translation of the gel; without it, the gel buckles and slips from between the anvils. It is believed that a combination of hydrogen bonding between the gel and the cellulose in the wipe and capillary forces due to porosity is responsible, so any paper product with some degree of porosity should also work.

III.2. Electrical Behavior of Electrically Conducting Hydrogels

The resistance behavior of a compressed conductive hydrogel was established and was used as a baseline for comparing the behavior of the lattice hydrogels. It was thought that the lattices might exhibit a strain-rate invariant resistance, since the strain rate had little effect on the stress-strain behavior (Figure 3.7). A series of tests were performed to verify this, but unexpected features appeared in the resistance curves. All data is preliminary and requires further investigation.

III.2.1. Electrical Test Setup

Electrical resistance measurements were recorded with a Keithley (2400 series) source meter through a custom script in Test Script Builder. An initial direct current of 0.01 A was applied while measuring the voltage. The script instructed the source meter to reduce the current by an order of magnitude when the voltage reached a threshold of 2 V. This was because the hydrogels would begin to offgas if the voltage got too high, so a voltage limit well below that point was selected (2 V). The source meter recorded time, current, voltage and resistance, and was programed to stop recording once the resistance has reached a selected maximum value (indicating sample failure). The time data is matched with the timestamp of the mechanical data to track changes in resistance with strain.

For the solid samples, the four-point probes were connected, via alligator clips, to a pair of copper plates that were attached to the anvil plates. In between the copper plates and the anvils was a layer of masking tape and double-sided tape. The masking tape served to insulate the copper plates from the testing machine, and the double-sided tape attached the copper plates to the anvils. The tissue paper was not required for the solid samples, as they did not slip during testing. During the mechanical and electrical testing, the sample was placed between the copper plates to bridge the circuit.

The electrical test setup for the lattices is still an ongoing investigation, which is discussed in section III.2.3. However, the setup is identical to the one used for the solid samples, except for the type of electrode, which is involved in the investigation.

Prior to any electrical tests, the circuit was bridged with a piece of copper tape to ensure that the resistance was low (~0.01 ohms) relative to the samples. Upon testing, the script and universal testing machine were initiated simultaneously, and the date was synchronized during analysis.

III.2.2. Solid vs. Lattice

Figure 3.9 shows how the resistance behaves for a solid and lattice as they are compressed to failure and 80% strain, respectively ($\dot{\varepsilon}$ = 100%/ min). The actual resistance values were not of interest for this experiment, just the change during compression, as the scope of the research was focused on understanding the behavior rather than optimizing values.
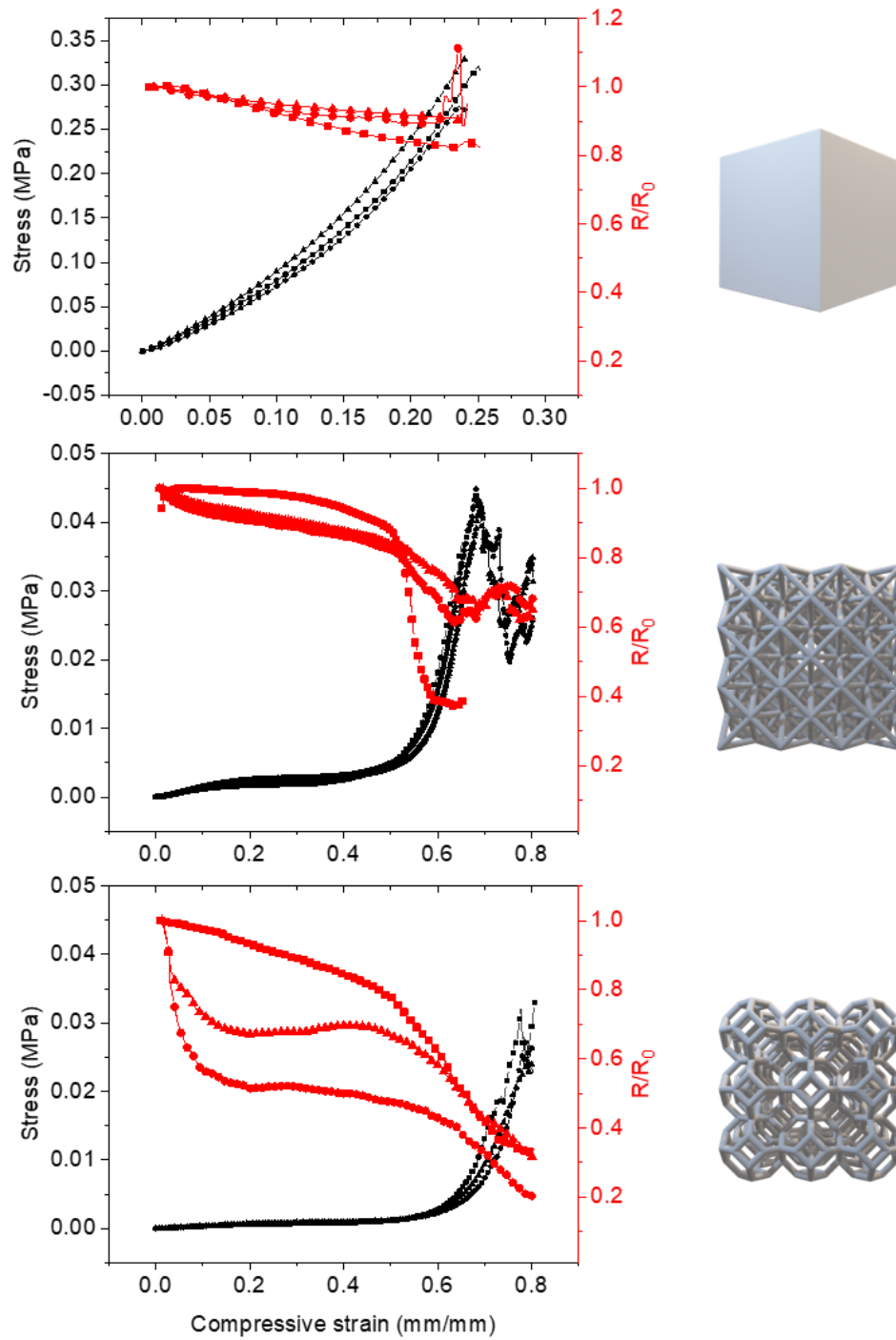
Figure 3.9. Stress-strain-resistance curves for a solid, octet and truncated octahedron, respectively. Note the different scales for solids and lattices. The red curves represent the normalized electrical resistance of three samples, identified by their symbol, and correspond with the compressive stress-strain curves (black).

The resistance curves of the solid were quite repeatable and displayed good overlap. There is a slight downward trend as the solid gel reaches its fractures point. This could be a result of the polyaniline network developing more pathways for conduction as it is pushed closer together. The lattice, however, exhibits a resistance curve that is almost an inverse of the stress-strain curve. The plateau region of the resistance curve was of interest, as it is believed to offer constant resistance over a larger region of strain compared to the solid, and within a region of elastic deformation. In addition, the results of the strain rate compression tests suggested that the resistance may also exhibit strain rate invariance, which are topics of interest for future studies.

However, as one can see by the collection of resistance curves, the degree of change throughout compression differs widely, despite all sharing a plateau region. The initial drop in resistance in the beginning was also a source of uncertainty. It was believed to be caused by inadequate contact between the electrodes and lattice and was further investigated.

III.2.3. Electrical Contact Investigation

The solid samples could be placed directly onto a copper plate and undergo compression without any concern of slipping. The lattices were not as straightforward. The challenge was finding a way to make good electrical contact while also preventing any slipping during compression. The substrate used for securing the lattices for mechanical testing was an insulating paper material (tissue paper), but the material used for measuring the resistance of the solids was a slick metal, copper. Initial attempts were made by cutting a hole in the tissue paper and placing it on top of the copper plates to allow the lattice to contact both the tissue paper and copper plate simultaneously. Over time, the tissue paper became saturated with water from the samples and began to tear. It was replaced each time, but the tearing was probably happening during compression, which led to the belief that there was some contact issue causing the initial sloped region of the resistance curve.

The next attempt to resolve the contact issue involved coating coarse sandpaper with silver paint. The idea was that the sandpaper would hold the lattice in place and the silver paint would be a conductive coating. This ultimately did not fix the issue, and the silver paint became unstable over time as a result of water soaking into the sandpaper.

One attempt to solve the contact issue utilized carbon cloth as the electrodes. The carbon cloth worked well to prevent slipping, but the resistance curves still had the initial sloped region, and exhibited uncharacteristic shapes not seen in any previous tests with the other electrode types.

Another strategy was to use a copper mesh as the electrode (**Figure 3.10**). The copper mesh had the advantage of being conductive while also being able to prevent slipping. The coarse braids made of intertwined copper wires provided grip via their serrated-like pattern and coarse texture. The data gathered using the copper mesh electrodes had mixed results (**Figure 3.11**). Some curves had almost no initial slope and some did. It was discovered afterwards that the timestep used to measure resistance (t = 0.2 s) was too large for the higher strain rates, potentially leading to a loss of temporal resolution, which would be why the curves do not exhibit the initial slope or plateau region. A simple adjustment of the script should fix the issue. However, another issue appeared from the same series of tests. The plateau region, which was the initial motivation for the tests, exhibited a distinct linear decline, something not previously observed. It is not exactly clear why this happened, but there was evidence of some reaction occurring on the cathode surface (**Figure 3.12**), which is something that has been observed during previous static measurements of resistance of solid gels. The cause then was determined to be high HCl loading within the solid gel. It is possible that the samples were not fully rinsed of HCl when processed.
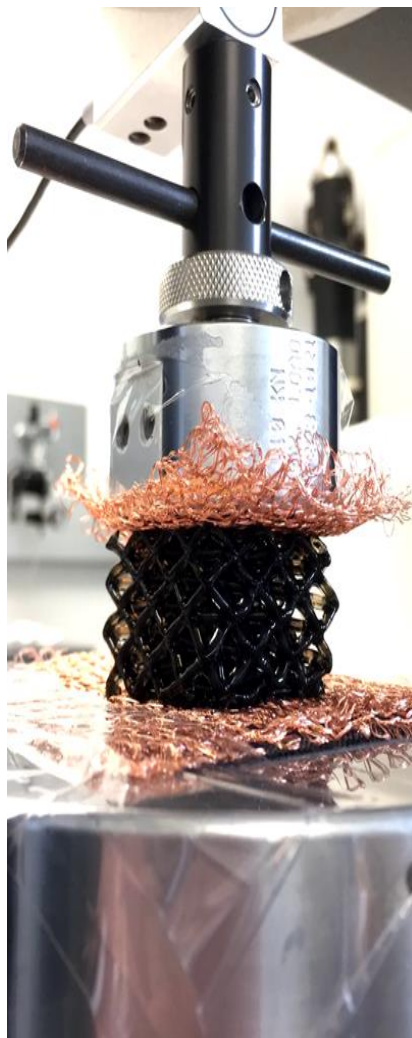
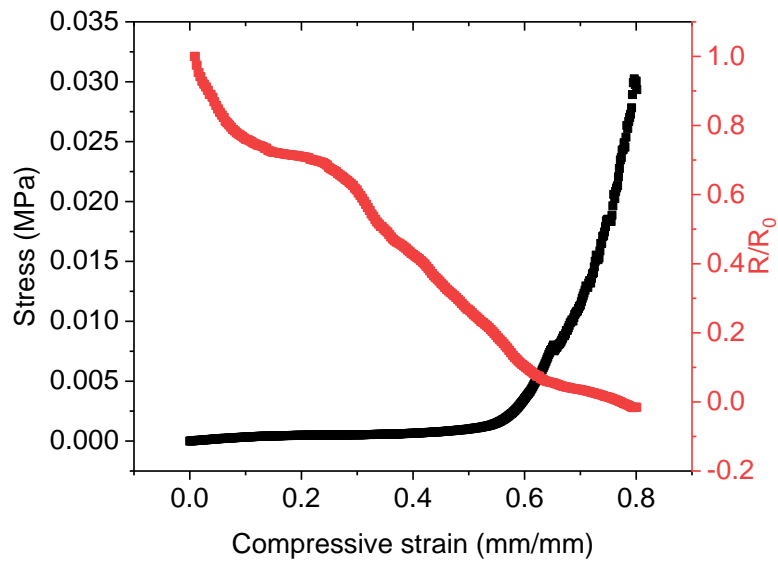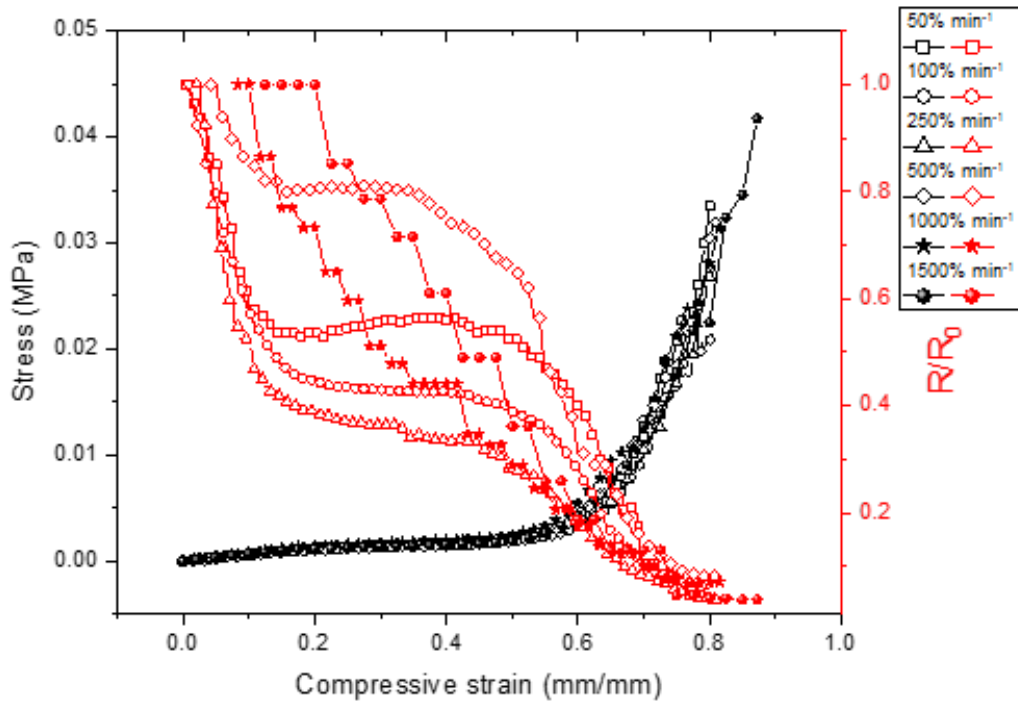**Figure 3.10**. Copper mesh electrode setup.

Figure 3.11. Stress-strain-resistance curves of lattices obtained with the copper mesh electrode. Top) The loss of resolution of the resistance curve as the strain rate increases. Bottom) A resistance curve that has a linear decline where a plateau usually exists. Also exhibiting a negative resistance, which the cause is not known. Further investigation is required.

Figure 3.12. Suspected corrosion of copper mesh indicated by the darker spots.
Note: pictured here is a troubleshooting setup and not the setup used for testing.

References

1. M.F. Ashby, A.G. Evans, N.A. Fleck, L.J. Gibson, J.W. Hutchinson and H.N.G. Wadley, *Metal Foams: A Design Guide*, Butterworth-Heinemann, Woburn, MA, **2000**.

2. N. A. Fleck, V. S. Deshpande, and M. F. Ashby*, Proc. R. Soc. A.* **2010**, *466, 2495–2516.*

3. A. Gross, P. Pantidis, K. Bertoldi, and S. Gerasimidis, *Journal of the Mechanics and Physics of Solids,* **2019**, *124, 577–598.*

4. J. U. Surjadi, L. Gao, H. Du, X. Li, X. Xiong, N. X. Fang, and Y. Lu, *Adv. Eng. Mater.* **2019**, *1800864.*

5. V. S. Deshpande, M. F. Ashby and N. A. Fleck*, Acta mater.* **2001**, 49, 1035–1040.

IV. Towards Architected Solid-state Electrically Conducting Polymers

One of the future goals is to achieve a solid-state lattice conducting polymer. The lattices in this work were 95-98% water by mass, which can be used for applications requiring a hydrated environment like supercapacitors and batteries but is not suitable for solid electronics. The issue of water evaporation would also need to be addressed with some form of encapsulation or carefully controlled humidity. As of now, removing water from a 3D printed hydrogel of desired architecture is the most promising approach, due to lack of compatible photochemistry. A preliminary experiment was performed to replace the water in the gel with glycerol of 20 wt.% and 40 wt.%, which was calculated using the mass of the dry hydrogel. Glycerol has a much lower vapor pressure than water and would serve as a plasticizer to conducting polymers once water is completely removed.

IV.1. Weight Percent Determination

The wet lattices were removed from their water filled container and patted dry to remove as much residual water as possible. Their wet masses were recorded, and the gels were left to dry at room temperature over a period of a couple of days. Once dry, the masses were recorded again to obtain the masses that would be used for the weight percent calculations. The dry mass was subtracted from the wet mass to obtain the mass of the water initially within the lattices. The ratio of the mass of the water to the mass of the glycerol for each weight percent was used as the concentration of a solution of water and glycerol. The idea was that if the lattices were placed into a solution of the determined concentration of glycerol and water, the lattices would swell with the same concentration; and when dried, they would lose the water but retain the glycerol. And since the glycerol concentration was calculated based on solid polymer weight percentages, the remaining glycerol would match the mass of the desired weight percent. An example calculation is shown below.

Obtain the mass of the water:

$$M_{water} = M_{wet} - M_{dry}$$

Use the mass of the dry gel for weight percent calculations (20 wt.% shown):

$$M_{glycerol} = M_{dry}(0.2)$$

Use the mass of the water in the gel and the mass of the glycerol to make a mass ratio for the water/ glycerol solution:

$$\frac{M_{water}}{M_{glycerol}}$$

An example calculation:

$$M_{water} = 10.12\ g - 0.266\ g = 9.855\ g$$

$$M_{glycerol} = 0.266\ g(0.2) = 0.053\ g$$

$$\frac{M_{water}}{M_{glycerol}} = \frac{9.855g}{0.053\ g} \approx 186$$

Where the mass ratio of water to glycerol is 186:1.

Assuming the ratio holds when the gel is swelled, when the water in the gel evaporates, the amount of glycerol that remains should be near $M_{glycerol}$.

IV.2. Mechanical and Electrical Properties

Like with the previous samples, the lattices with glycerol underwent a compression test while the resistance was measured. The motivation for the test was to get a sense of the behavior of the plasticized gels in comparison to their hydrated counterpart. 20 and 40 wt.% samples of a truncated octahedron and octet were tested (**Figure 4.1**). It is important to note that this data is preliminary and not to be analyzed quantitatively. It should instead be thought of as a glimpse of the potential of the solid-state conductive hydrogels. The mechanical and electrical behavior seen in the hydrated lattices is also seen in the plasticized lattices (**Figure 4.2**). The plasticized lattices also showed no signs of any beams breaking when compressed up to 80-percent strain, whereas the hydrated lattices did during compression in the densification zone. However, the plasticized lattices were too sticky to recover due to the amount of glycerol within them. Once the concentration of the glycerol is optimized, the gels should exhibit greater recoverability.
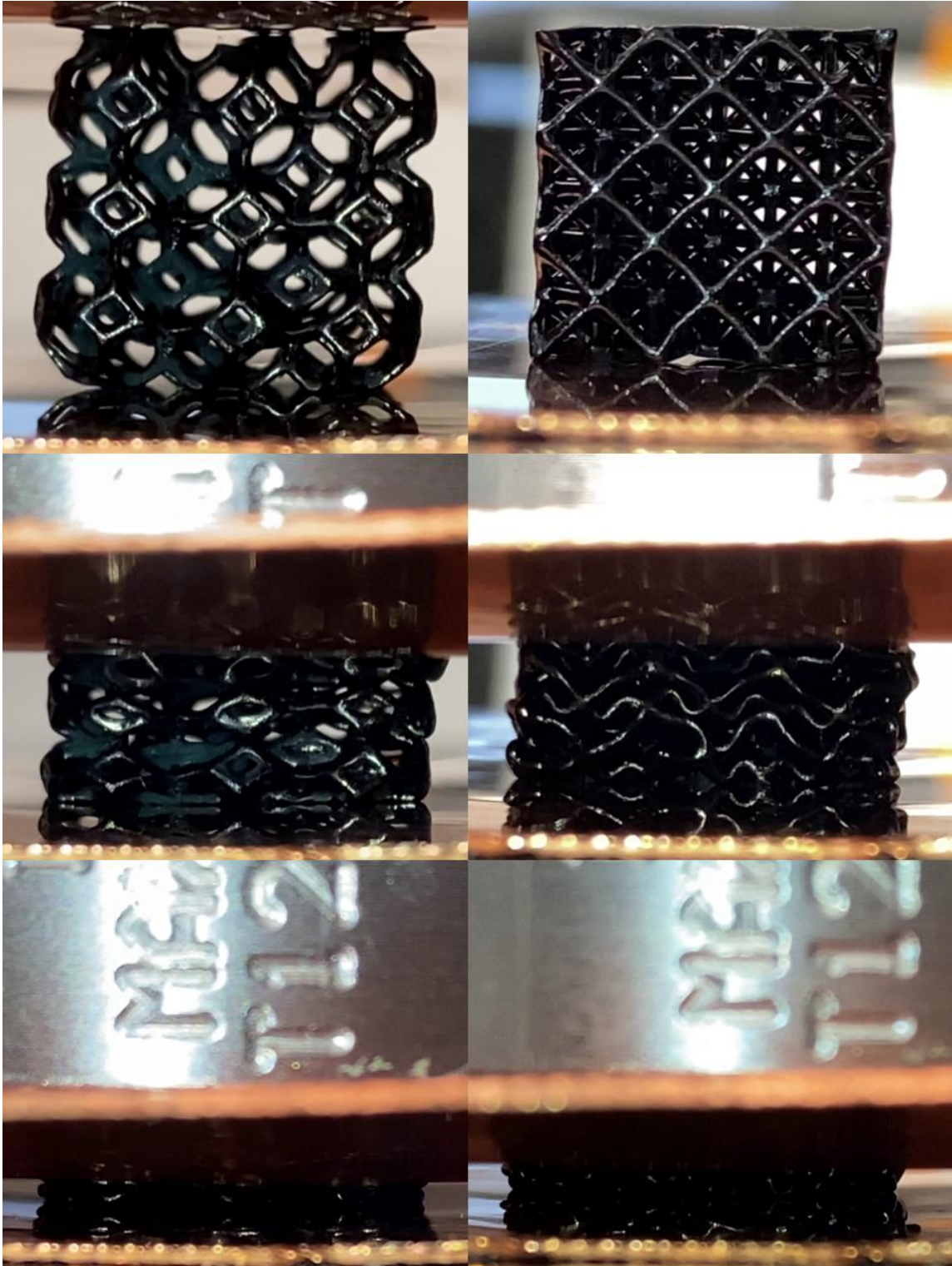
Figure 4.1. Solid-state truncated octahedron (left) and octet (right) in their mechanical-electrical test configuration being compressed to various strains (from top to bottom).
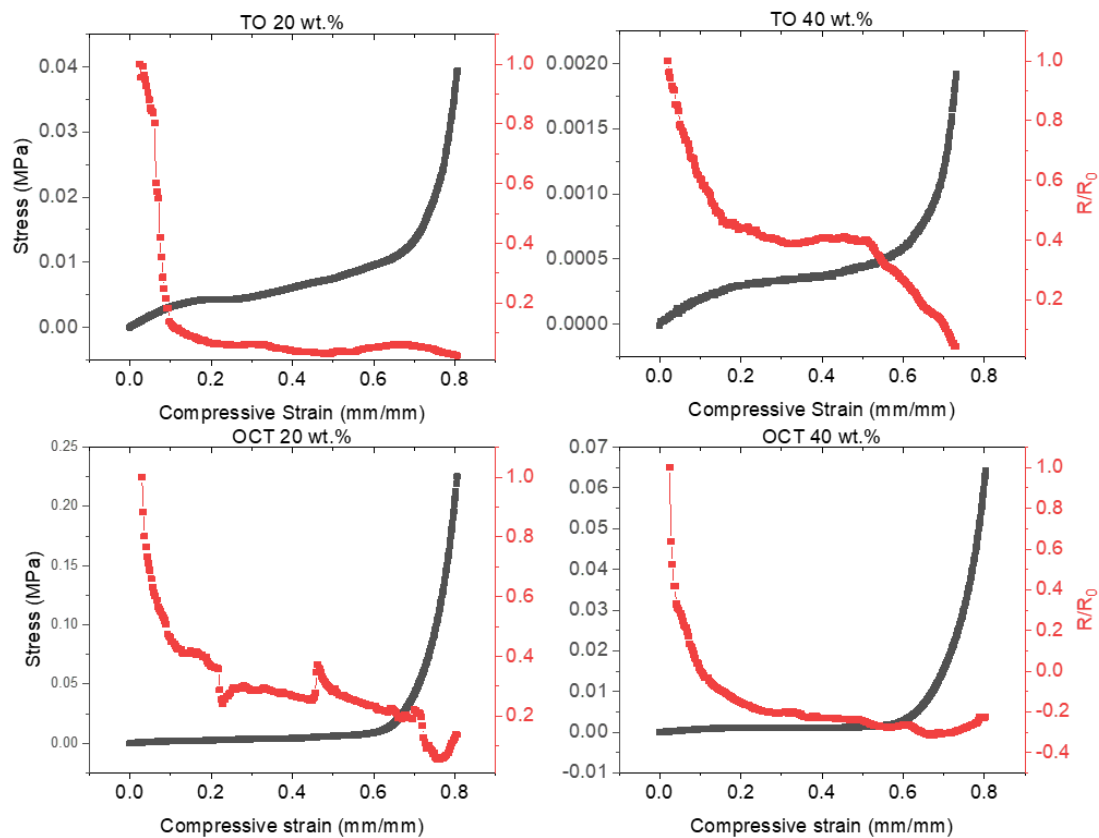
Figure 4.2. Compressive stress-strain-resistance curves of solid-state truncated octahedra (TO) and octets (OCT). *Note: this is preliminary data. Graphs are an aid to visualize general behavior of samples and the issues with the electrical data collection. Data was collected before density problem was fixed, and contact issue is still not resolved (see R-curve of OCT 40 wt.%)*

V. Conclusion and Outlook

Much progress was made over the course of this project. First and foremost, a reliable system for 3D printing a conducting polymer-based hydrogel has been established. Any object that can be made with a commercial 3D printer can now be made with a conducting polymer. The preliminary characterization results light a pathway for future exciting research. And the early-stage solid-state conducting polymer lattices show promise of future exciting applications.

However, there is still much work to be done. There are three things that need to be addressed for the mechanical characterization. First, it is hypothesized that the spot size of the laser is larger than the spot size being used in the slicer program. This is problematic because it leads to inaccurate sample densities. An experiment should be performed to first determine the actual spot size. Once the spot size has been measured, adjustments should be made to the slicing program. Based on the acquired knowledge on SLA printing, it is not advisable to print a hydrogel of a single line width, as it would be nearly impossible to measure due to its fragility and uncertain dimensions due to swelling. The second thing that should be addressed is the build plate size. The sheer number of samples required to carry out the mechanical and mechanical-electrical study render the current build plate, as well as the experimenters, overburdened. A larger one should be made.

The third and most critical part that needs further investigation is the initial slope of the resistance curves generated by the lattices. It was originally thought to be a result of poor contact between the lattice gels and electrodes, but the behavior persisted after using various electrode types. It may be useful to investigate if the water on the surface of the gel plays any role. It may also be useful to use an SEM to view the microstructure of the conducting polymer network as it transitions from the surface to the interior of the gel. Additionally, some samples showed a negative resistance towards the end of their compression. It occurred in both hydrated and solid-state samples; the cause is not known. Further investigation is required.

Finally, the solid-state conducting polymers show great promise with no yielding up to 80% strain, but the samples tested contained too much glycerol and stuck together when compressed. It is believed the method used to swell gels with glycerol is viable, but it needs to be optimized. More weight percentages should be tried, and a database of all the masses should be made.

The project has concluded with achievement of the first goal of establishing a reliable 3D printing system that can make a conducting polymer into any desired 3D shape. The viability of architected lattice materials' role in tailoring the mechanical properties of a conducting polymer has been shown. Promising preliminary mechanical data point in the direction of facile tailorable conducting polymers. An unexpected strain-rate-invariant

response has been discovered in the lattices and suggests that their electrical resistance may also be strain-rate-invariant over a large degree of strain and strain rate. And finally, preliminary data show a robust solid-state conducting polymer may be within reach.